

# Shallow water equations on spherical multiple-cell grids

Jian-Guo Li

Met Office, Exeter, UK

Email: [Jian-Guo.Li@metoffice.gov.uk](mailto:Jian-Guo.Li@metoffice.gov.uk)

18 June 2025

## 1. Overview of various spherical grids

The latitude-longitude grid is the most widely used global coordinates for various purposes, and it is still the favoured grid in global numerical models. Despite of its known polar problems, it is still used in many operational and research models for its simplicity and convenience. With the increase of data assimilation in operational models, its convenience becomes even more obvious or more indispensable. Apart from the singularity at the poles, the most troublesome polar problem associated with the lat-lon grid is its converging meridians or diminishing longitude grid length towards the poles, which leads to a severe Courant-Friedrichs-Levy (CFL) time-step limit on Eulerian advection schemes. Since the start of numerical modelling in the 1960s, two major classes of approaches have been developed to tackle this polar problem: one is the introduction of reduced grid, and another is switching to semi-Lagrangian advection schemes. The reduced or skipped grid with multiple-increment of longitude mesh was first introduced by Gates and Riegel (1962) and a quasi-uniform reduced grid was created by Kurihara (1965) to tackle the lat-lon grid CFL restrictions. These grids have obviously relaxed the CFL limits at high latitudes but introduced another problem, that is, the scalar assumption of vector components defined by the local east reference direction over the increased longitude grid-length. Because the local east direction changes with longitude, the scalar assumption becomes invalid near poles due to the increased longitude mesh stride. For instance, if a row has only 4 cells around the pole on a reduced grid, the local east direction changes  $90^\circ$  over one grid length, which leads to complete mix-up of the north and east velocity components among neighboring cells. So numerical errors were found larger in the polar regions than near the Equator, particularly in reduced grids. Shuman (1970) demonstrated that the polar errors are due to the increased curvature of the parallels near the pole and the reduced number of points along the parallels. Williamson and Browning (1973) compared finite difference models of shallow water equations (SWEs) on the standard uniform latitude-longitude grid and the Kurihara skipped grid and concluded that this scalar assumption error is not necessarily the case with true scalar quantities and the increased errors near the poles with vector variables on the skipped grid can be significantly reduced when additional longitudinal grid points are added in the polar regions. This is also true in spectral-transform models on quasi-uniform reduced grids (Hortal and Simmons 1991, Courtier and Naughton 1994, Williamson and Rosinski 2000) where more grid points are required near the poles than the original quasi-uniform grid to suppress the truncation errors in the polar regions. These early studies on reduced grids failed to appeal due to the large errors induced by the increased curvature in the polar regions with vector variables. The reduced grid was calumniated for this error and was almost abandoned in finite difference models (Staniforth and Thuburn 2012).

Switching to a semi-Lagrangian advection scheme is a successful approach for solving the polar problems on the lat-lon grid, which avoids the CFL restriction on Eulerian transport schemes in the polar regions. McDonald and Bates (1989) introduced a rotated grid in the neighbourhood of a pole to trace the departure points for their semi-Lagrangian transport scheme because the latitude-longitude grid could not be used to trace the departure points in the polar regions due to the increased curvature. They also found large polar errors in the momentum equations due to the same reason as the model variables are kept on the original latitude-longitude grid. Subsequent improvement along this line (such as Kent et al 2016) has made the semi-Lagrangian approach a favourite choice on the latitude-longitude grid. One disadvantage of the semi-Lagrangian scheme on the latitude-longitude grid is that it requires significant data communication among the grid points clustered around the poles and this leads to a bottleneck in modern parallel computing (Staniforth and Thuburn 2012). If semi-Lagrangian scheme could be implemented on a reduce grid, it might relax this communicating burden.

Other global grid options have also been studied in order to replace the latitude-longitude grid and they lead to abundant literature works on various global grids, such as the icosahedral-hexagonal Voronoi grid (Sadourny et al 1968), geodesic grid (Williamson 1968), quasi-uniform cubed spherical grid (Sadourny 1972, Nair et al 2005), finite element triangular grid (Cullen 1974), twisted icosahedral grid (Heikes and Randall 1995, Giraldo et al 2002), conformal cubed (Rancic et al 1996) or octagonal (Purser and Rancic 1997) grids, Yin-Yang overset grid (Kageyama and Sato 2004), and the pineapple-alike Fibonacci grid (Swinbank and Purser 2006), quasi-uniform

octagonal grid (Rancic et al 2008), to list a few. Qaddouri et al (2012) compared different discretizations of SWEs on three spherical grids (the global latitude-longitude grid, the overset Yin-Yang grid, and the finite-volume geodesic icosahedral grid) and concluded that all three models are competitive in accuracy, but the latitude-longitude grid has larger noises in the polar regions than the Yin-Yang grid. The icosahedral grid model is the poorest among the three. Weller et al (2012) studied computational modes and grid imprinting on five quasi-uniform spherical C-grids and concluded that all the five grids suffer from computation modes that are usually associated with triangles in the primal or dual grid. The skipped latitude-longitude grid performs almost perfectly when the flow is aligned with the grid and well when the grid is rotated. But relatively large errors occurred in the polar region, and they attributed the increased errors to the merged cells or changed resolutions. A more detailed review of those various horizontal grids was given by Staniforth and Thuburn (2012) and they stated that all known grids have their own problems or issues, and quadrilateral grids are generally preferred to other grids (triangles, pentagons or hexagons) due to extra numerical modes present on non-quadrilateral grids. Peixoto and Barros (2013) studied geodesic grid imprinting errors and indicated that cells of even numbered edges (such as quadrilaterals and octagons) are better than odd-edged cells (such as triangles and pentagons). Although the latitude-longitude grid is not geodesic, it is as accurate as an even-edged geodesic grid for second order discretization of the divergence.

Variable or multi-resolution grids are on the rising recent years. St-Cyr et al (2008) explored the quad-tree based block-structured adaptive grid technique on the latitude-longitude and cubed-sphere grids. The model is adapted from the finite-volume SWEs model of Lin and Rood (1997). Polar filter is applied to the momentum equations to stabilise the fast waves originated from the pressure gradient terms. Each block is surrounded by ghost cells for boundary conditions and those ghost cells are updated by neighbouring blocks. Weller et al (2009) used cell averaged velocity and height as the main prognostic variables and included quasi-prognostic face fluxes to control grid-scale oscillations of the A-grid. They tested four variable resolution grids (hexagonal and triangular icosahedral, cubed sphere and reduced lat-lon grid) each with a doubled resolution disc area of a radius of 25° centred at 30°N. They found resolution refinement could introduce errors and degrade the global accuracy. They also showed that reduced latitude-longitude grid gives very good accuracy when the flow is aligned with the mesh. Ringler et al (2011) tested SWEs on variable resolution meshes which are spherical centroidal Voronoi tessellations and concluded that the solution error is controlled primarily by the grid resolution in the coarsest part of the model domain and is attributed to the increased truncation error in the coarse region. Düben et al (2012) discretized the viscous and inviscid shallow water equations on icosahedral geodesic grids with hybrid finite element methods. Düben and Korn (2014) extended this study on variable resolutions and concluded that grid refinement does not deteriorate geostrophic balance and turbulent cascades. No spurious behaviour is visible at transition zones except for waves of the same order of magnitude as the grid spacing.

The spherical multiple-cell (SMC) grid (Li 2011) is a compromise between the structured latitude-longitude grid and unstructured global grid. It is adapted from the Cartesian multiple-cell unstructured grid (Li 2003) and combined with the longitudinal merging like a reduced grid. As it uses the latitude-longitude grid quadrilateral cells, numerical modes are minimised and the simple finite-difference schemes on latitude-longitude grids are retained. It also supports quad-tree like mesh-refinement (Berger and Oliger 1984) but is more flexible than the original one because of its unstructured feature. As a result, this grid is useful for resolving refined coastlines and small islands (Li 2012). To tackle the vector polar problem associated with the increased curvature at high latitudes, SMC grid uses a new fixed reference direction to define vector components near the poles (Li 2012, 2016). This guide will present the SWEs on the SMC grid and demonstrate that the reduced grid can be reclaimed if the vector polar problem is properly handled.

## 2. Discretization of global shallow-water equations

Following Ringler et al (2010), the nonlinear SWEs can be written in a vector-invariant form:

$$\begin{aligned} \frac{\partial h}{\partial t} + \nabla \cdot (h\mathbf{v}) &= \nabla \cdot (\kappa \nabla(h + b)) \\ \partial \mathbf{v} / \partial t + \eta \mathbf{k} \times \mathbf{v} + g \nabla(h + b) + \nabla K &= 0 \end{aligned}$$

where  $h$  is the fluid thickness or the water column height,  $t$  the time,  $\nabla \equiv \mathbf{i} \frac{\partial}{r \cos \varphi \partial \lambda} + \mathbf{j} \frac{\partial}{r \partial \varphi}$  the horizontal gradient operator,  $\mathbf{v} = u\mathbf{i} + v\mathbf{j}$  the fluid horizontal velocity on the earth's surface,  $\kappa$  is a diffusivity coefficient used to smooth down small-scale oscillations,  $\mathbf{i}$  and  $\mathbf{j}$  the horizontal unit vectors of a local Cartesian coordinates,  $\mathbf{k}$  the local vertical unit vector,  $r$  the radius of the Earth,  $b$  the bottom topography,  $g$  the gravity constant,  $\varphi$  the latitude,  $\lambda$  the longitude,  $K = |\mathbf{v}|^2/2$  the kinetic energy,  $\eta = \xi + f$  the absolute vorticity,  $f = 2\Omega \sin \varphi$  the Coriolis

parameter,  $\Omega$  the angular spinning speed of the earth, and  $\xi = \mathbf{k} \cdot \nabla \times \mathbf{v}$  is the relative vorticity. The momentum equation should be modified for the polar regions due to the invalid scalar assumption at high latitudes. A fixed map-east direction as shown is then introduced in the polar region to define the vector components. The map-east system in the polar region can be approximated with a rotated grid with its rotated poles on the Equator. The conversion between the two direction systems is a simple rotation of the velocity components.

The continuity equation can be discretized straightforward on the SMC grid as a scalar advection-diffusion equation as in Li (2011) if the water thickness is located at the cell centre and normal velocities on cell faces (C-grid). The UNO2 scheme (Li 2008) can be used to determine thickness fluxes so it is estimated by

$$h^{n+1} - h^n = -\frac{\Delta t}{A} \sum_s F_s^* L_s$$

where the superscript  $n$  represents the  $n$ -th time level,  $\Delta t$  denotes the time step,  $A$  is the cell area,  $F_s^*$  the combined advection-diffusion thickness mid-flux through the cell side  $s$ , and  $L_s$  the length of the cell side. The summation is over all sides of the given cell so resolution changing side is automatically considered by the side length. The UNO2 advection scheme is of 2<sup>nd</sup> order accuracy despite of combining with the first order forward time difference (Li 2008). The diffusion term is a central-in-space scheme, which is also of 2<sup>nd</sup> order accuracy. However, the diffusion term makes the 2<sup>nd</sup> order advection scheme equivalent to a first order scheme.

Discretization of the momentum equations is the trickiest part in SWEs models. The mass transportation scheme is based on a C-grid velocity field (normal velocity component on cell faces) while the kinetic energy and potential energy gradient terms require the two velocity components to be at the same point as the thickness variable or on a A-grid. To make things even complicated, the vorticity is best to be evaluated with D-grid velocity components (tangential velocity components on cell faces). So SWEs model is always a compromise among these requirements. For instance, Lin and Rood (1997) presented a finite volume model on a D-grid and integrated the C-grid velocity components on a half-timestep for mass transportation. This mixed CD-grid system is more expensive than deriving the C-grid velocity by interpolation of the D-grid fields, but it is chosen to avoid the 2-grid waves in the interpolation scheme. Although the model is based on a full latitude-longitude grid, a polar cap (cell) idea was introduced to tackle the singularity at the Pole. Weller et al (2009) used cell averaged velocity and height (A-grid) as the main prognostic variables and included quasi-prognostic face fluxes to control grid-scale oscillations of the A-grid. They concluded that the schemes perform well if skew-symmetry is maintained for spatial interpolation and temporal treatment of the Coriolis term is appropriate. Here the A-grid discretization is followed, that is, the velocity components are at the same cell centre as the thickness. The potential and kinetic energy can then be calculated directly from the prognostic variables and the momentum equation becomes

$$(\mathbf{v}^{n+1} - \mathbf{v}^n)/\Delta t = -\eta^n \mathbf{k} \times (\mathbf{v}^{n+1} + \mathbf{v}^n)/2 - \nabla(gh^{n+1} + gb + K^n)$$

For stability purpose, both the absolute vorticity term and the potential energy gradients are approximated by semi-implicit schemes. Because the thickness is calculated with an explicit scheme, the  $n+1$  time level thickness can be treated as an explicit term. Decomposing the momentum equation into local Cartesian component form and solving for velocity components, we have

$$\begin{aligned} (1 + \beta_n^2)u^{n+1} &= u^n + \beta_n(2v^n - \beta_n u^n - G_y^{n+1}) - G_x^{n+1} \\ v^{n+1} &= v^n - \beta_n(u^{n+1} + u^n) - G_y^{n+1} \end{aligned}$$

where  $\beta_n \equiv \eta^n \Delta t / 2$  and the  $x$ - and  $y$ -direction gradients of the total energy can be expressed as

$$G_x^{n+1} \equiv \Delta t \mathbf{i} \cdot \nabla(gh^{n+1} + gb + K^n)$$

$$G_y^{n+1} \equiv \Delta t \mathbf{j} \cdot \nabla(gh^{n+1} + gb + K^n)$$

In low latitudes, the component direction will be the same local east as in the latitude-longitude grid. In the polar regions the momentum equation retains the same form except for that the gradient components are projected to the map-east system instead of the local east system.

As it is crucial to get the Coriolis parameter right in the absolute vorticity estimation (Walters et al 2009), the Coriolis terms are calculated with the prognostic cell centre velocity while the relative vorticity is converted into a cell side loop integration (the Stokes theorem) with interpolated velocities on cell sides. The relative vorticity loop integration is then approximated as a polygonal cell side summation:

$$\xi = \mathbf{k} \cdot \nabla \times \mathbf{v} \approx \frac{1}{A} \sum_s \mathbf{v}_s \cdot \mathbf{s}_t$$

where  $\mathbf{v}_s$  is the velocity on the cell side  $s$ ,  $\mathbf{s}_t$  is the side length tangential vector that follows an anticlockwise circle around the given cell,  $A$  the area of the cell and the summation is over all the cell sides of the given cell.

As SMC grid mass transportation requires the normal velocity components on cell faces while the vorticity integration needs the tangential velocity components on cell faces, the cell centre velocity components solved with the A-grid momentum equation could not be used directly for the mass transport and vorticity integration. The cell centre velocities are then interpolated on cell faces, including both the normal and tangential velocity components. The cell centre thickness is used as a weight in this interpolation:

$$\mathbf{v}_s = (h^+ \mathbf{v}^+ + h^- \mathbf{v}^-) / (h^+ + h^- + \varepsilon)$$

where  $h^{+/-}$  is the thickness for the down (+) and upper stream (-) cell of the given cell side and  $\varepsilon$  is a negligibly small non-zero value to avoid zero-dividing when both cells have zero water height. As the velocity components are in the fixed direction system in the polar regions, the component interpolation can be done as a true scalar interpolation at high latitudes without worrying about the increased curvatures. The interpolated face velocities, however, must be rotated into the local east system in the polar regions because the cell sides are aligned with the local east and north directions as in the latitude-longitude grid. The weighted velocity interpolation approximates the depth integrated method of Kleptsova et al (2009) for stability with variable bathymetry.

The kinetic energy can be estimated directly with the cell centre velocity as  $K = (u^2 + v^2)/2$  and then added to the updated potential energy for a combined gradient term. Calculation of the scalar energy gradient term requires a different formulation in the polar regions as the cell centre velocity components directions are in the map-east system rather than the cell face normal directions (in local east system). The total energy gradient term is first calculated in the local east system on each cell face and then rotated to the map-east system in the polar regions before they are averaged for the cell centre gradients, that is,

$$G_x^{n+1} = \Delta t \mathbf{i} \cdot \nabla E \approx \frac{\Delta t}{L} \sum_s \mathbf{i} \cdot \mathbf{s}_n \frac{E_+ - E_-}{d_{+-}}, \quad E \equiv gh^{n+1} + gb + K^n$$

Where  $\mathbf{s}_n$  is the side length normal vector (pointing from cell - towards cell +),  $L$  the total side length of the summed sides for the given cell,  $E_{+/-}$  the energy of the two cells sharing the given face and  $d_{+-}$  the distance between the two cell centres. The gradient component direction vector,  $\mathbf{i}$ , is the local east unit vector at low latitudes but changes to the map-east direction in the polar regions. For stability reason, it is important to use the  $n+1$  time step potential energy ( $gh^{n+1}$ ) for the energy gradient. This is done by simply integrating the thickness equation first before calculating the gradient term. The accuracy of the discrete momentum equation is overall of first order accuracy despite of the gradient term is central-in-space or 2nd order. The forward time difference and vorticity integration are generally of first order accuracy. Higher order time difference and integrations are available but are not attempted here for simplicity.

There is a known instability problem associated with the cell face velocity interpolation from A-grid velocity (McDonald and Bates 1989, Lin and Rood 1997, Weller et al 2009) despite of using weighted interpolations. Besides, false gravity waves could be generated due to mismatched representations of physical fields in numerical models (Mohebalhojeh and Dritschel 2000). So, an extra smoothing is needed to control the numerical small-scale oscillations and spurious gravity waves. For instance, McDonald and Bates (1989) introduced a divergence damping term into the momentum equation for this purpose and Weller et al (2009) used extended cell averaging and polar filters. In this model a 1-2-1 weighted local average in each dimension is applied for the velocity components. The average is equivalent to a diffusion term with a Fourier number of 1/4 for one time step. For easy control of the damping effect, the average is called at a given interval rather than every time step. The average interval is selected to be just short enough for suppressing numerical instability, so it varies in different tests, depending on the nature of the test flow. The average can also be applied more often in the polar regions to act as a polar filter than at low latitudes for normal smoothing. To match the extra polar smoothing of the velocity components, the diffusivity coefficient used in the thickness equation can be specified as a polar-biased variable of the latitude:

$$\kappa = \kappa_m (1 - \sigma + \sigma \sin^2 \varphi), \quad \kappa_m \leq \Delta x_{min}^2 / (2\Delta t), \quad 0 \leq \sigma \leq 1$$

where  $\sigma$  is a tuneable parameter to control the polar-bias and  $\kappa_m$  is the maximum diffusivity at the poles, which is limited by the stability requirement depending on the minimum grid length  $\Delta x_{min}$  and timestep  $\Delta t$ .

Boundary conditions may vary for different models. For ocean surface wave models the zero-boundary condition is required at coastlines. For a global model, a periodic condition is usually applied in the longitude direction. The SMC grid is originally developed for global wave models and the coastal zero-boundary and the global periodic conditions are built into the face arrays. This approach effectively changes any boundary face into an equivalent inner face so that a single loop covers all faces. The periodic boundary condition is applied by linking the end cell with the start cell at one parallel circle in the face array. The zero-boundary condition at coastlines is achieved by bounding each coastal cell face with an empty cell in its face array. If external boundary conditions are required at domain edges, they can be applied directly on selected boundary cells with an extra boundary condition loop, just like in a conventional structured grid.

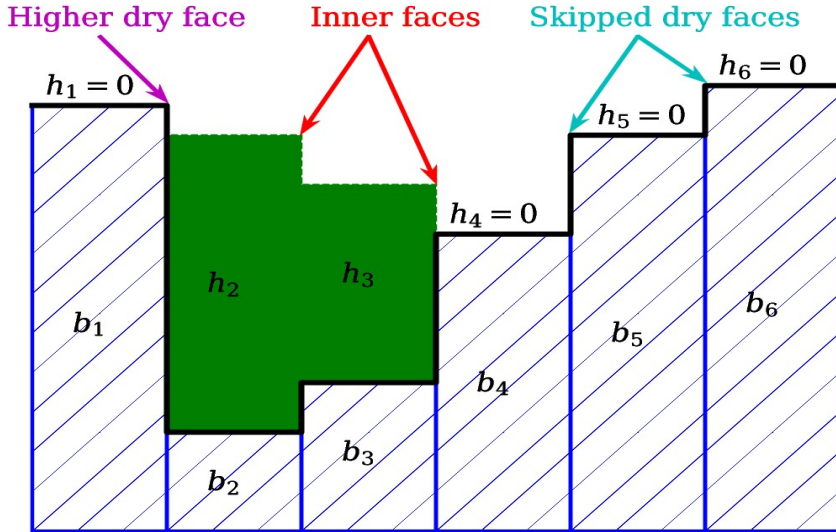


Fig.1. SWEs model boundary classification.

For the SWEs model, vertical wall or closed boundary conditions are applied at coastlines. Flux through any coastal cell face is set to be zero so no mass or momentum emerge, if any when the inner cell is wet, could leak out of the inner cell through the boundary face. This is done by setting the normal velocity to be zero at coastal boundary faces so no water can leak through these real boundary faces. For this reason, any possible flooding zone must be included in the SMC grid. For example, the sea surface grid could be extended to coastal area up to 10 m above sea level for possible storm surges in the coastal region. Tangential velocity components at boundary faces are set to be equal to their inner cell centre velocity component if the inner cell is wet. This boundary tangential velocity setting ensures momentum energy will not leak through boundary faces. To simulate flooding, any cell in this SWEs model is enabled to flip between wet and dry status as coastlines may move with flooding waters. The cliff wall boundary conditions are extended for inner faces if required for this purpose. A cell is deemed wet when its cell centre water height is positive (or  $h > \varepsilon$ ); otherwise, it is treated as a dry cell. Velocity is set to be zero at a dry cell centre without solving the momentum equation. Any inner face bound by two dry cells (will be referred to as a dry face) is simply skipped in face loops as illustrated in Fig.1. This is equivalent to treating the area covered by the two dry cells as land area. If a cell face is bound by a wet cell and a dry cell and the cell floor is higher than the wet cell water level, it will be treated as a vertical wall boundary face and referred to as a higher dry face in Fig.1. If the dry cell floor is lower than the wet cell water level, the face is considered a normal inner face just like any wet face bounded by two wet cells. This ensures water from the wet cell can flow into the lower dry cell under gravity. The wet to wet and wet to lower dry faces are marked as inner faces in Fig.1.

Cliff wall boundary conditions are extended to those higher dry faces. The cell side velocity interpolation is modified for the higher dry faces by setting the normal velocity component to be zero and the tangential component to be equal to the value at the wet cell centre. This is equivalent to the cliff wall boundary condition applied to all coastal faces. The energy gradient term is set to be zero at higher dry faces, so the net momentum flux is zero across these boundary faces. The weighted 1-2-1 average for the momentum equation is limited among wet cells to avoid energy dissipation into dry cells. This tangential velocity assignment and zero-energy gradient on the higher dry boundary faces ensures the Hollingsworth instability (Hollingsworth et al., 1983) is avoided. Water mass advection fluxes through the higher dry faces are also zero because the normal velocity component is zero. The mass diffusion flux is only calculated between wet cells and hence the diffusion flux through a higher dry face is also zero. These zero advection and diffusion fluxes through higher dry faces ensure water mass is confined

within low area. Otherwise, water mass might be numerically pumped into higher dry cells, violating the common sense that a lake at rest has a mirror flat surface.

For global grid with polar regions, the boundary faces beyond the polar region linking zone must be treated differently from the cliff-wall boundary condition. Zero-gradient boundary condition is applied to these linking zone boundary faces. To distinguish the linking boundary faces from the lateral boundary faces, the linking zone boundary faces will be bounded by the cell with index = 0 while lateral boundary faces will be bounded by cells with negative indexes (-1 to -9).

An additional forcing term, the bottom friction, is added to the momentum equation and it takes the simple form as used in Lyard et al (2006) global tidal model:

$$\mathbf{B}_{Frc} = -C|\mathbf{v}|\mathbf{v}/h$$

where  $C$  is a dimensionless constant,  $\mathbf{v}$  the horizontal velocity and  $h$  the water depth. As the bottom friction coefficient  $C$  is on the order of 1.0E-3 and ocean current speed is generally below 1 m s<sup>-1</sup>, the bottom friction term has little effect on the current in deep oceans. It may have some impact in shallow waters and coastal runups. This term can be discretized with a linearized semi-implicit scheme. The  $C|\mathbf{v}|$  part is valued with the  $n$ -th time level velocity while the remaining  $\mathbf{v}/h$  is estimated with  $n+1$  time level velocity and water depth. As a result, it appears as a linearised term in the momentum equation.

The SWEs model is parallelized with OpenMP for shared memory systems at present, which reduces the model runtime by over 50% with 2 or 3 OpenMP threads on the same desktop machine in comparison with single processor model runs. Further parallelization is required for distributed memory supercomputers in hybrid MPI-OpenMP mode.

### 3. Tests of the model on a full global grid

The main test grid is shown in Fig.2. It is a SMC 1° global grid plus a refined ¼° area between about 14°E and 84°E in longitude and from 15°N to 50°N in latitude. The actual mesh increments are  $\Delta\varphi_1 = 0.25^\circ$  and  $\Delta\lambda_1 = 360^\circ/1024 = 0.3515625^\circ$  for the finest mesh in the refined area. The longitudinal increment is chosen so that merged cells at high latitudes are exact multiples of the finest one. The base resolution (size-4 cell) is 1° only in the latitudinal dimension while the base resolution longitude mesh increment varies from about 1.4° on the Equator to 45° on the last row before each polar cell. This 3-level multi-resolution grid will be referred to as the SMC1°MR3 grid. Two single resolution SMC grids are also used for comparison purpose: one is the same as the SMC1°MR3 grid except for that the refined area is replaced with base-resolution cells; another single resolution grid uses an increased base resolution of  $\Delta\varphi_2 = 0.5^\circ$  and  $\Delta\lambda_2 = 360^\circ/512 = 0.703125^\circ$ , which is equal to the size-2 cell in the SMC1°MR3 grid. The first single resolution grid will be referred to as the SMC1° grid while the half degree single resolution grid will be referred to as the SMC1°/2 grid. The red circle in Fig.2 marks the fixed reference direction zone in the polar regions to tackle the increased curvature there. Because of the two reference systems used for vector variables, the low latitude part must be separated from the two polar regions. For this purpose, four overlapping rows, as indicated by the red and yellow rings, are added to link up the low latitude part and each polar region with two-way boundary conditions. The outmost two rows of each part are updated each timestep with corresponding values from the other part, after appropriate vector rotation. Extra zero-gradient boundary conditions are applied to each part beyond their own boundaries to reduce boundary effects on the two parts. Note that the global SMC grid appears the same as the reduced grid of Weller et al. (2009), but the numerical schemes are different. Their reduced grid is treated as a special case of polygon mesh and hence the polygon schemes are used.

#### (a) Steady zonal flow

The steady zonal flow test suggested by Williamson et al (1992 test case 2) is a classical one and is widely used by other modellers. If the steady flow rotation axis passes the rotated grid poles, the global steady zonal geostrophic flow velocity and initial thickness are given by

$$u = u_0 \cos\varphi, \quad v = 0, \quad gh = gh_0 - u_0(\Omega r + 0.5u_0)\sin^2\varphi$$

where the parameters are chosen as  $gh_0 = 2.94 \times 10^4$  m<sup>2</sup>s<sup>-2</sup> or  $h_0 \approx 3000$  m,  $u_0 = \Omega r/12$  and  $\Omega$  is the angular rotation speed of the Earth. The rotation axis is chosen to have a given angle  $\alpha = 0.05$  or  $\pi/2 - \alpha$  from the grid north pole so that the effect of grid orientation on the zonal flow can be studied. The top panel in Fig.3 shows the

initial thickness field on the SMC1°MR3 grid for the  $\pi/2 - 0.05$  case. The rotated north pole is at (2.865°N, 180°E) or about 3° from the grid equatorial surface. This experiment will be referred to as W203 test for short.

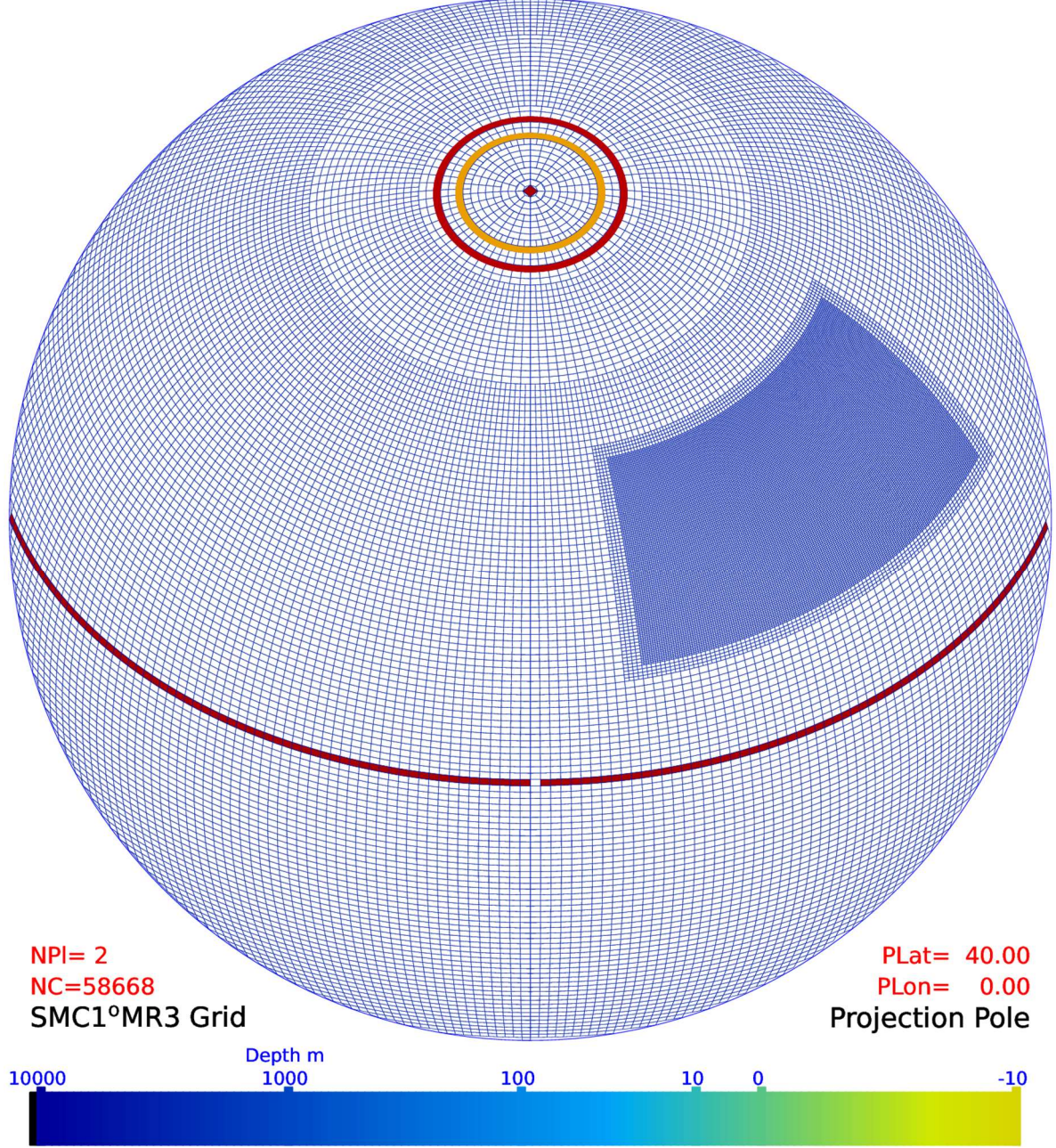


Fig.2 The SMC1°MR3 grid

Time step is set to be 90 s and the velocity average is called every half hour of model time. The thickness diffusion coefficient is set to be  $\kappa_m = 3.5 \times 10^5 \text{ m}^2\text{s}^{-1}$  and  $\sigma = 0.4$ . The diagram is drawn by cell-by-cell polygon-filling with height colour rounded to the nearest 254 colour levels between 800 and 3600 m and the projection is the same as in Fig.2. The bottom panel in Fig.3 shows the difference between the initial field and the simulated W203 thickness field after 5 model days, which uses 254 colour levels between -28 and 28 m. The model retains the initial zonal thickness field well except for a slight slowdown of the rotation due to numerical dissipation and smoothing. As a result, the maximum thickness decreased from the initial 3000 m to about 2993 m and the minimum thickness increased from 1095 m to 1112 m after 5 days. The thickness field is smooth over the whole globe except for some 2-grid ripples in the polar regions and near the boundaries of the refined area, indicating that the numerical schemes and the two reference directions for vector variables are working well. The half-hour velocity average and polar biased thickness diffusion are roughly enough to suppress the numerical noises.

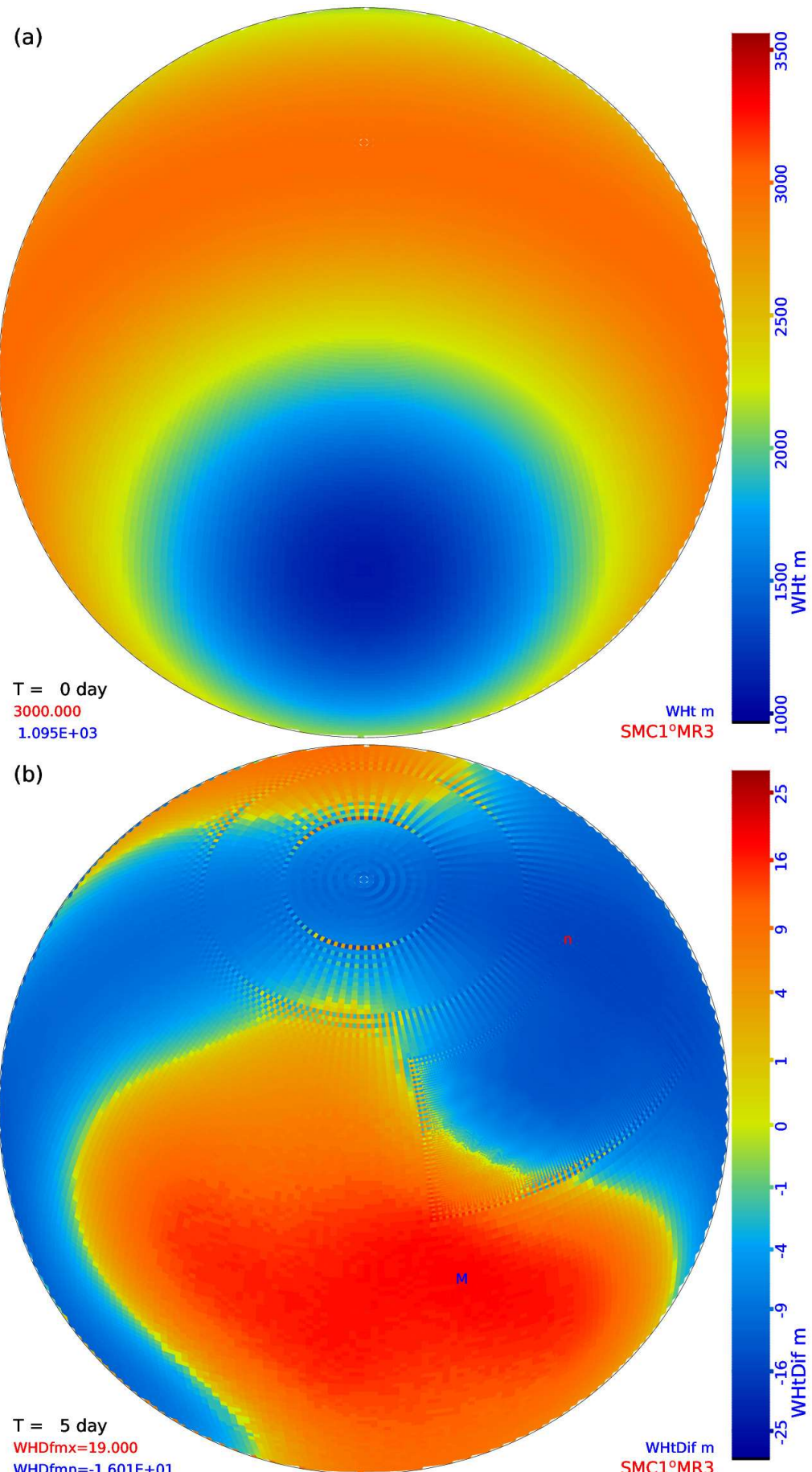


Fig.3 W203 initial water height and the difference after 5 model days.

The magnitudes of those small 2-grid waves are no more than 19 m as shown by the maximum and minimum differences in Fig.3. These small-scale waves could be further reduced by increasing the diffusivity and average but at the cost of further slowdown of the flow.

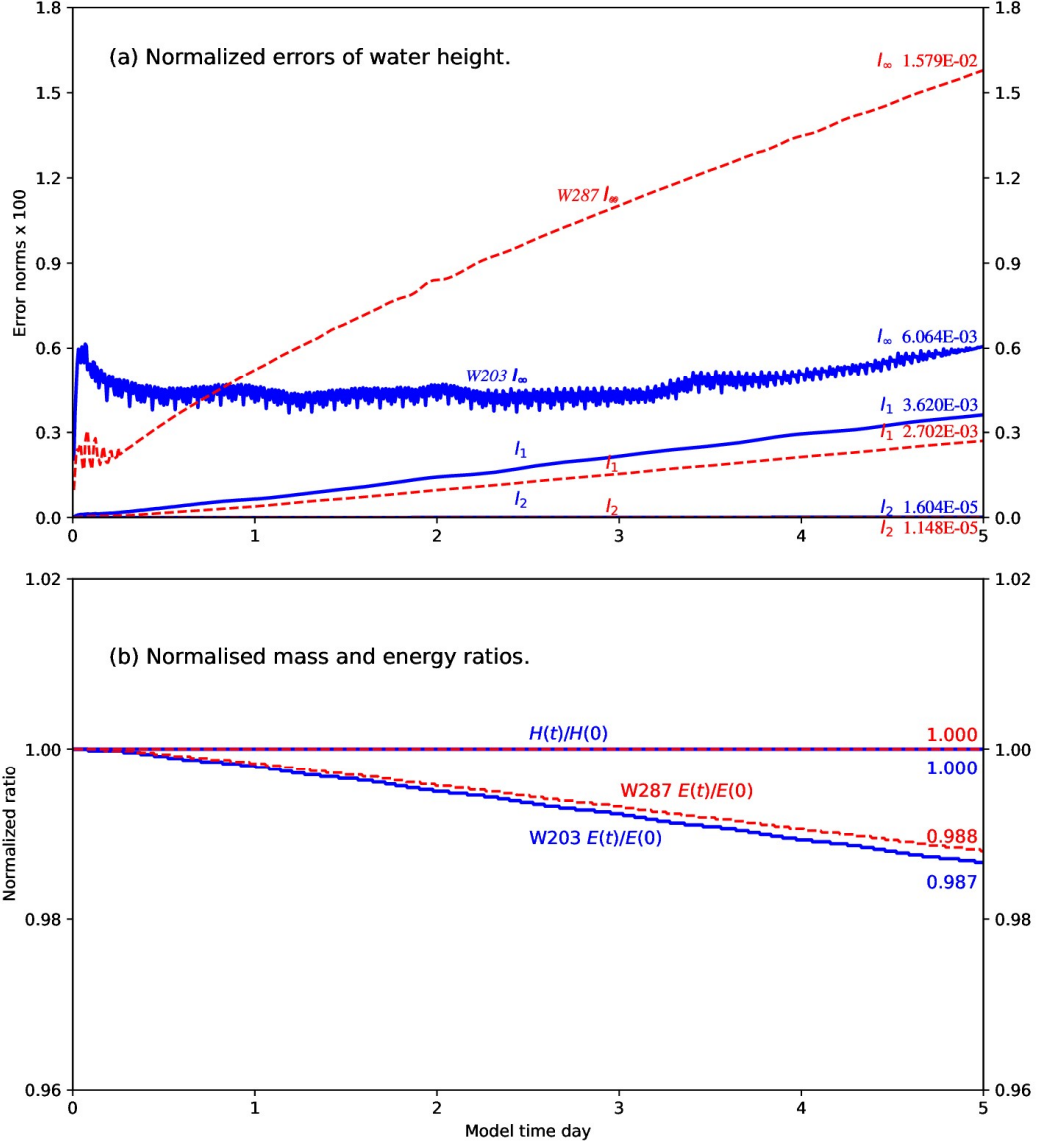


Fig.4 W203/287 error norms  $l_1$ ,  $l_2$ ,  $l_\infty$  and normalized mass and energy.

The other test with the same model configurations as in W203 but  $\alpha = 0.05$  or the rotation north pole at  $(87.135^\circ\text{N}, 180^\circ\text{E})$  is also carried out and it will be referred to as W287 test. The W287 result is slightly better than that of W203 and the main reason for the improvement is because the velocity aligns with the grid better in W287 than in W203 and hence reduced numerical dissipation. This agrees with other works in the literature (such as, Weller et al 2012).

Williamson et al (1992) introduced some global measures of the errors of any simulated variable  $\psi$  against its true value  $\psi_T$  with integrations over the whole model domain. Three normalized errors are defined as

$$\begin{aligned} l_1(\psi) &= I[|\psi - \psi_T|]/I[|\psi_T|] \\ l_2(\psi) &= I[(\psi - \psi_T)^2]/I[\psi_T^2] \\ l_\infty(\psi) &= \text{Max}[|\psi - \psi_T|]/\text{Max}[|\psi_T|] \end{aligned}$$

where  $I[\psi]$  stands for the integration mean of  $\psi$  over the whole model domain, and  $\text{Max}[\psi]$  is the maximum value of  $\psi$  among all values within the model domain. For this zonal flow test, the initial field will be the true field and

the water height error norms for the two tests are shown in Panel (a) of Fig.4. The W287 errors are smaller than those of W203 except for the  $l_\infty$ . The error norms at the end of 5 model days are marked with their values. Note that the  $l_2$  norms are hardly discernible due to the large-scale differences from the other two error norms, so their end values are printed beside their mark points. The  $l_2$  norms after 5 days are 1.15E-5 for W287 and 1.60E-5 for W203. The increased  $l_\infty$  error in W287 is due to the extra polar smoothing so the minimum water height increased from the initial 1095 m to 1138 m after 5 days, about 26 m higher than that of W203 (1112 m). The maximum height after 5 days in W287 is 2993 m, almost the same as that of W203 test. The oscillations of  $l_\infty$  error in W203 test indicate that the maximum values happened to be the grid oscillations. Small oscillations also appear in W287 but the maximum values are at near the poles, not showing the oscillations.

Panel (b) in Fig.4 compares the mass and energy ratios of these two tests to their initial integrated values, respectively. The integrated total energy decreases steadily with time in both tests due to the model numerical dissipation. The dissipation rate of the W203 test is slightly larger than that of W287. After 5 model days, the total energy ratio is reduced by about 1.2% in W287 and 1.3% in W203. Finite difference methods in dynamical models have inherent diffusions which may help dissipate potential enstrophy and prevent the build-up of kinetic energy at the grid scale, but this inherent diffusion also leads to dissipation of total energy. Mass is conserved by the flux-form advection-diffusion scheme used in the thickness equation and this is confirmed by the total mass integration, which remains constant throughout the model run in both tests.

#### (b) Immersed hill test

The test case 5 suggested by Williamson et al. (1992) – W5 test hereafter – used the same initial conditions as in case 2 but retuned the parameters and immersed below the water surface a cone-shaped hill defined by

$$h_s = H(1 - r_s/R), \quad \text{for } r_s = \sqrt{(\lambda - \lambda_c)^2 + (\varphi - \varphi_c)^2} \leq R.$$

The parameters are chosen as  $H = 2000\text{m}$ ,  $R = \pi/9$ ,  $\lambda_c = 3\pi/2$ , and  $\varphi_c = \pi/6$ . The parameters for the steady zonal flow are different from those in case 2 and they are chosen to be  $\alpha = 0$ ,  $h_0 = 5960\text{ m}$  and  $u_0 = 20\text{ m s}^{-1}$ . The initial water height is given by subtracting the immersed hill  $h_s$  from the initial steady flat-water surface, that is,

$$gh = g(h_0 - h_s) - u_0(\Omega r + 0.5u_0)\sin^2\varphi.$$

The time step is set to be 30 s for this test and global average is called every 40 min model time. Three more extra polar averages (above  $73^\circ$ ) are applied between the global averages to act as a polar filter for suppressing polar gravity waves. The thickness diffusivity is unchanged  $\kappa_m = 9.0 \times 10^6 \text{ m}^2\text{s}^{-1}$  but  $\sigma$  is set to be 0.3 for a polar biased smoothing. Fig.5 shows the initial thickness field plus the cone hill height and it is a perfect zonal distribution with a maximum thickness of 5960 m on the Equator and a minimum of 4992 m at the poles. The location of the immersed hill is marked with its footprint by the dotted circle and the refined area by the dotted rectangle. The background colour is filled cell by cell using 254 colour levels between 4900 and 6100 m. Fig.5 (b) shows the cone height plus the model simulated thickness field after 15 model days. Despite the gravity waves shown in the thickness field, the maximum thickness is reduced from the initial 5960 to 5941 m and the minimum thickness increased from 4992 to 5054 m. This is consistent with the energy dissipation in the steady zonal flow tests shown in the W2 tests. The underlying cone hill has stirred up gravity waves, which spread out to the whole globe. The enhanced polar average has helped suppress the polar gravity short waves and the relaxed global average has allowed the lingering of long waves at low latitudes. There is no analytic or true solution to this immersed hill test, but the result could be compared with other numerical solutions in literature, such as the Fig.4 in Lin and Rood (1997). The standard latitude-longitude projection is used in Fig.5 for the convenience of comparison with other simulations. By visual checking the results are very close to those of Lin and Rood (1997) except for the displacement of the immersed hill in this test.

#### (c) Rossby-Haurwitz wave

For the test case 6 of Williamson et al (1992) the Rossby-Haurwitz wave initial velocity field is non-divergent and given by the stream function

$$\psi = r^2\omega(\cos^4\varphi\cos4\lambda - 1)\sin\varphi$$

where  $r$  is the radius of the Earth and  $\omega$  is a constant angular velocity. The initial velocity field can be derived by definition  $\mathbf{v} = \mathbf{k} \times \nabla\psi$ , which yields

$$\begin{aligned} u &= r\omega\cos\varphi + r\omega\cos^3\varphi(5\sin^2\varphi - 1)\cos4\lambda \\ v &= -4r\omega\cos^3\varphi\sin\varphi\sin4\lambda \end{aligned}$$

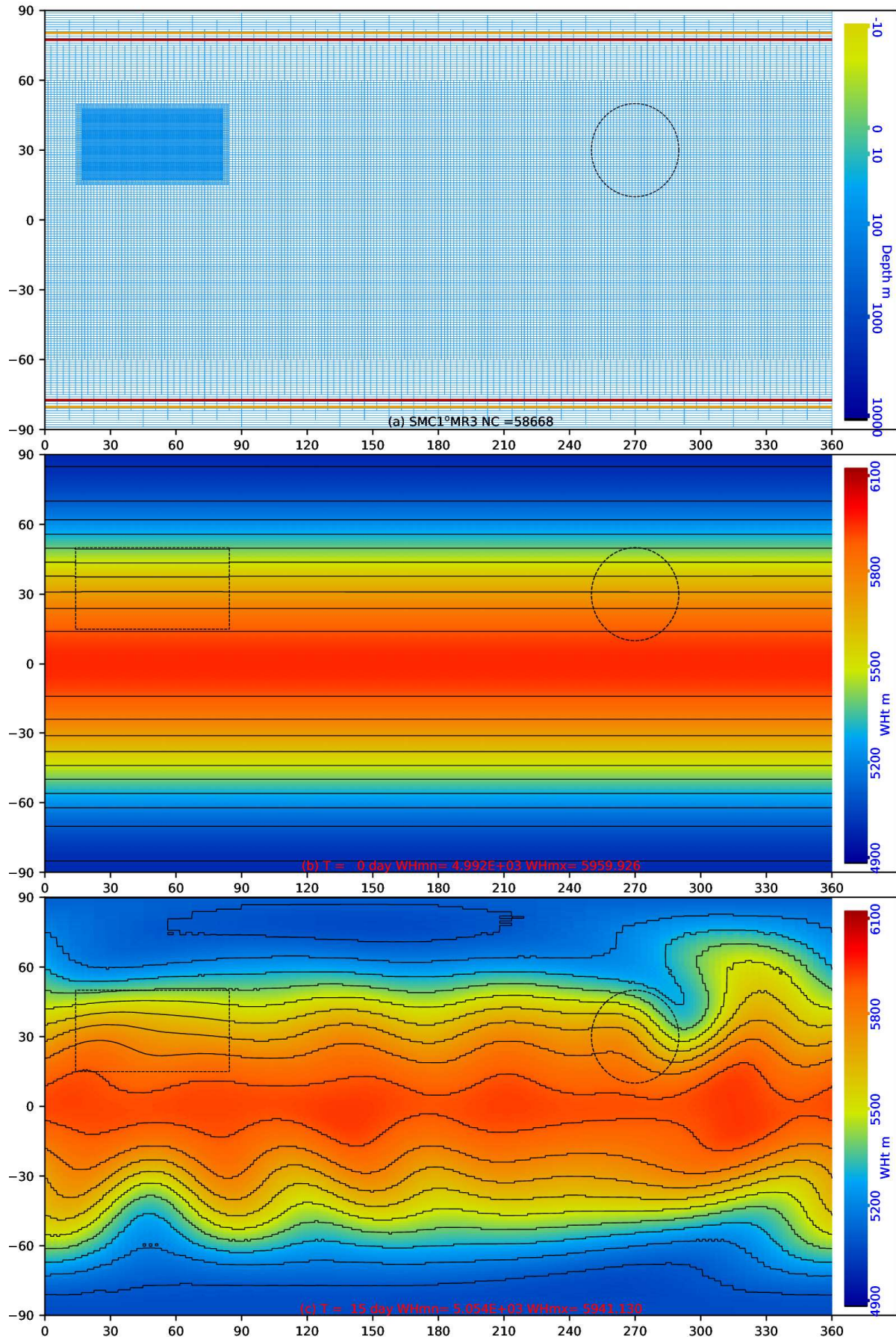


Fig.5 The SMC1°MR3 grid (a) and water height plus the merged hill at the start (b) and after 15 model days (c) in the W5 test.

The initial absolute vorticity can be obtained by inserting the velocity into the vorticity definition and we have

$$\eta = f + 2\omega \sin \varphi - 30\omega \cos^4 \varphi \sin \varphi \cos 4\lambda$$

The initial water height is obtained by solving the momentum equation and keeping the time differential and divergence to be zero:

$$(h - h_0)g/r^2 = (\Omega + \omega/2)\omega \cos^2 \varphi + (\omega^2/4)\cos^6 \varphi (5\cos^4 \varphi + 26\cos^2 \varphi - 32) + \\ (\Omega + \omega)(\omega/15)(1 + 25\sin^2 \varphi)\cos^4 \varphi \cos 4\lambda - (\omega^2/4)(1 + 5\sin^2 \varphi)\cos^8 \varphi \cos 8\lambda$$

The parameters are  $\omega = 7.848 \times 10^{-6} \text{ s}^{-1}$  and  $h_0 = 8000 \text{ m}$ . This initial pattern moves from west to east without change of shape in an ideal non-divergent barotropic model with an angular velocity,  $\omega_0 = (14\omega - \Omega)/15$ , which is about  $2.463 \times 10^{-6} \text{ s}^{-1}$  or  $12.19^\circ$  per day for the given  $\omega$  parameter and the Earth's angular speed  $\Omega = 7.2921 \times 10^{-5} \text{ s}^{-1}$ . Time step is set to be 30 s and global average is called every 40 min model time plus three polar ( $|\varphi| > 73^\circ$ ) average in between. The thickness diffusivity is set to be  $\kappa_m = 2.0 \times 10^6 \text{ m}^2 \text{s}^{-1}$  and  $\sigma = 0.25$  is chosen. The initial Rossby-Haurwitz wave thickness field on the SMC1°MR3 grid is shown by the panel (a) in Fig.6. The rectangle dotted lines mark the outlines of the refined area, and the contour increment is 200 m, starting from 7000 m. The background colour has 254 colour levels between 6900 and 11100 m and is drawn cell by cell. The initial thickness field has a perfect 4-wavelength zonal pattern. The model simulated thickness fields after 1 (b) and 7 (c) days on the SMC1°MR3 grid are shown by the (b) and (c) panels in Fig.6. After 1 model day, the wave pattern shown in panel (b) has shifted about  $12^\circ$  to the east in comparison with the initial condition in panel (a). Some dissipation or diffusion effect is already visible though the 4-wavenumber pattern is kept well. After 7 model days, the wave pattern shown in panel (c) has moved eastward by about  $85^\circ$  and been distorted by model error induced gravity waves. Note some small-scale oscillations are visible in the refined area, implying that the average and diffusion are not strong enough to remove them completely. The zonal flow has been weakened by numerical dissipation and the model averaging scheme, resulting in gradual decrease of pressure (thickness) gradient. The 4-wavenumber pattern starts to break down after 15 days and is eventually degraded into a zonal rotation flow by the numerical dissipation and the averaging effect. Thuburn and Li (2000) simulated the Rossby-Haurwitz waves using four different models and concluded that the zonal wavenumber 4 Rossby-Haurwitz wave is dynamically unstable and will eventually break down if perturbed or eroded by model errors. Higher resolution with lower truncation errors may retain the waves longer.

#### (d) Unstable zonal jet

Galewsky et al (2004) proposed an unstable zonal jet test. The initial zonal velocity, within the jet zone between latitude  $\varphi_0$  and  $\varphi_1$ , is given by

$$u(\varphi) = u_m \exp \left( \frac{4}{(\varphi - \varphi_0)^2} - \frac{1}{(\varphi_1 - \varphi)(\varphi - \varphi_0)} \right), \quad \text{for } \varphi_0 < \varphi < \varphi_1$$

Outside the jet zone the velocity components are set to be zero. The parameters are chosen as  $u_m = 80.0 \text{ m s}^{-1}$ ,  $\varphi_0 = \pi/7$ ,  $\varphi_1 = \pi/2 - \varphi_0$ , so that the jet's mid-point is located at  $\varphi_m = \pi/4$ . A balanced height field could be obtained by the integration:

$$h(\varphi) = h_0 - \int_{-\pi/2}^{\varphi} u(\varphi) [r \cdot f + u(\varphi) \tan \varphi] d\varphi$$

where  $r = 6371,220 \text{ m}$  is the Earth's radius,  $f = 2\Omega \sin \varphi$  is the Coriolis parameter, and  $h_0$  is a constant to be set so that the mean thickness of is 10,000 m. In this present grid estimation,  $h_0 \approx 10158 \text{ m}$ . To stir up a barotropic instability in this zonal jet flow, a localized bump is added to the balanced height field, and it is given by

$$h'(\varphi) = d_0 \cos \varphi \exp(-9(\lambda - \lambda_0)_m^2 - 225(\varphi - \varphi_m)^2), \\ (\lambda - \lambda_0)_m^2 = \min((\lambda - \lambda_0)^2, (\lambda \pm 2\pi - \lambda_0)^2)$$

where  $d_0 = 120 \text{ m}$  and  $\lambda_0 = 3\pi/2$ . Note the Gaussian perturbation function is multiplied by the cosine latitude factor to force the perturbation to be zero at the poles. The maximum disturbance height is about 85 m at about  $\lambda = \lambda_0$  and  $\varphi = \varphi_m = \pi/4$ . The  $\lambda_0$  value was set to be zero in the original test of Galewsky et al (2004) and relative vorticity field was displayed starting from  $90^\circ\text{E}$ . Here  $\lambda_0$  is shifted  $90^\circ$  to the west to avoid the refined area interfering with the initial disturbance. So, the vorticity plot starting from the zero meridian will be equivalent to the original one starting from  $90^\circ\text{E}$  in Galewsky et al (2004).

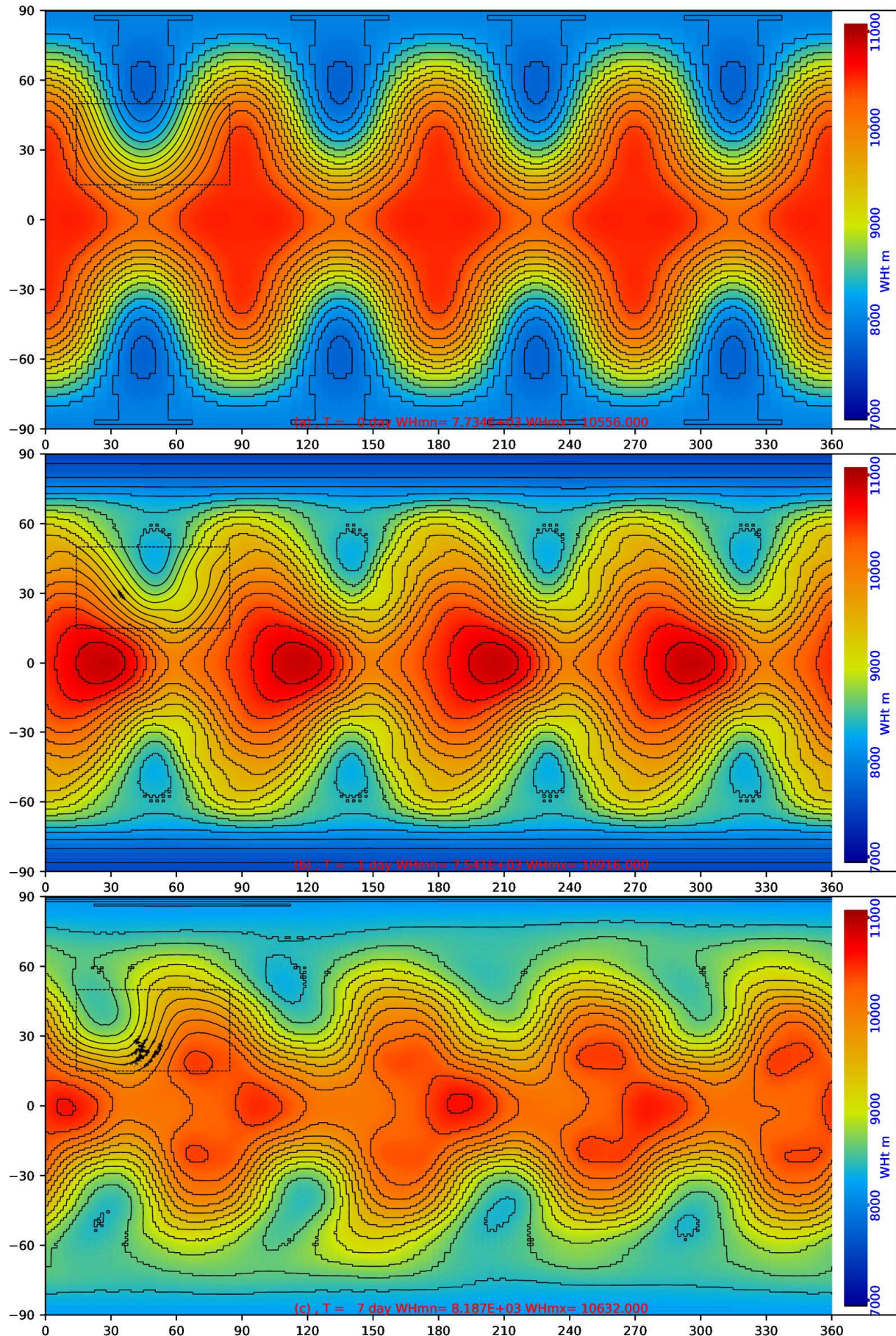


Fig.6 The thickness fields (a) at start and after (b) 1 and (c) 7 model days in the Rossby-Haurwitz wave test.

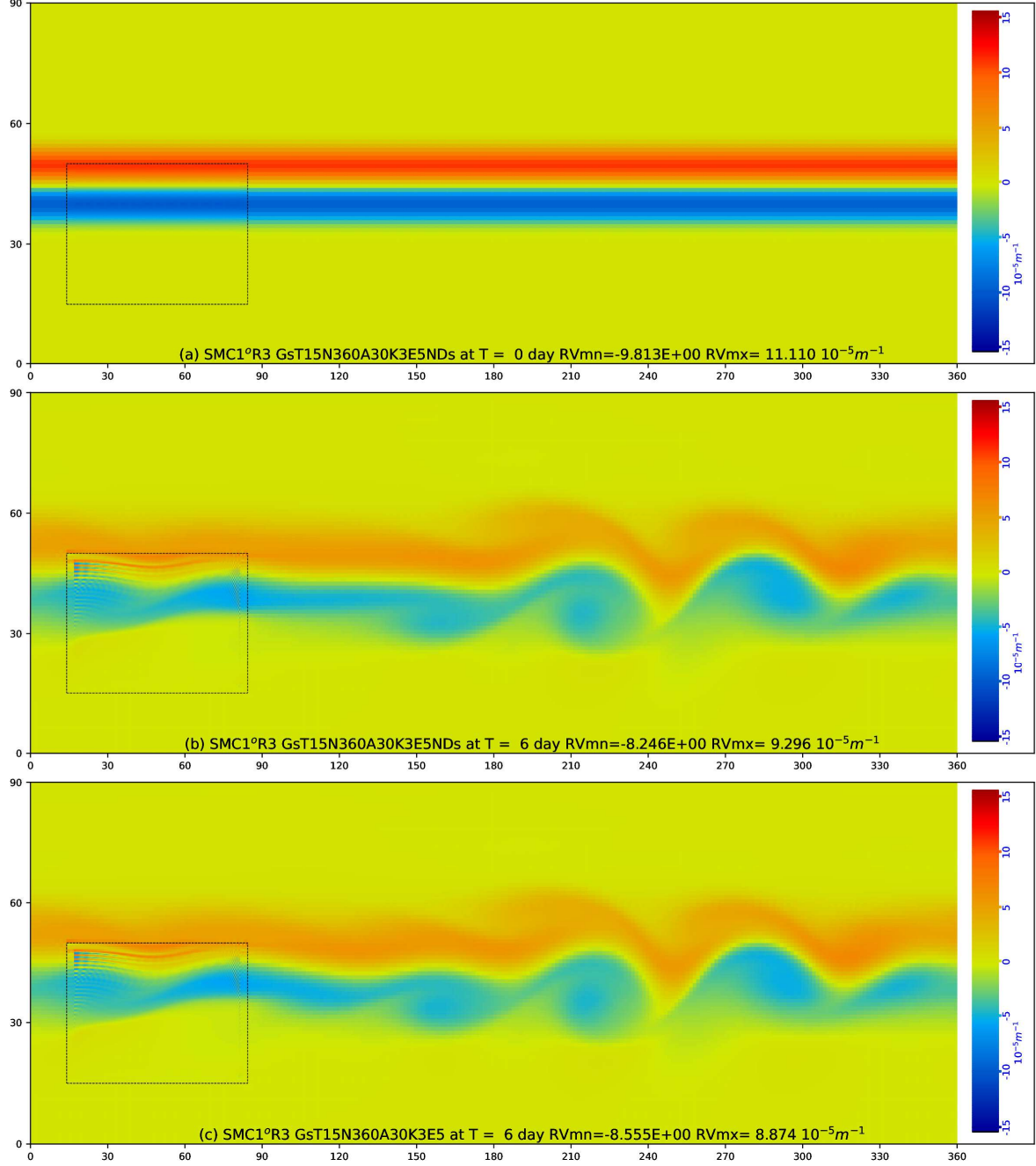


Fig.7 Relative vorticity fields at (a) start and after 6 model days (b) without the initial disturbance and (c) with it in the zonal jet test.

Duben et al (2012) pointed out that this unstable jet test is challenging for grid-point models because the narrow jet is fairly strong, and model errors induced perturbations may destabilise the jet and overshadow the intended small perturbation in the initial field. This is true for this multi-resolution grid. The panel (a) in Fig.7 shows the relative vorticity field at start, drawn cell by cell with 254 colour levels between  $\pm 1.51 \times 10^{-4} \text{ s}^{-1}$ . The unit for the relative vorticity is  $10^{-5} \text{ m}^{-1}$  in the figure. Only the north hemisphere is displayed here, and the dashed lines indicate the refined area, which is partially in the way of the strong jet flow as indicated by the non-zero vorticity colours. The other two panels in Fig.7 show the model simulated relative vorticity fields after 6 model days, one (panel b) excluding the intended initial disturbance and another one (panel c) when the disturbance is included. The refined area in the SMC1°MR3 grid has caused some instability or disturbance in the jet flow, which is large enough to stir up vorticity field changes almost as large as that of the intended initial disturbance. This is a bit of a surprise as this refined area is nearly unnoticed in previous tests. So, this test must have unveiled some hiding problem of grid refinement for strong jet flow. The timestep is set to be as small as 15 s and the average is relaxed to every 360 timesteps or every 1.5 hr model time to retain the vorticity changes. Polar average is added 10 times between global ones or every 30 timesteps to keep the model stable. The thickness diffusivity is set to be  $\kappa_m =$

$3.0 \times 10^5 \text{ m}^2\text{s}^{-1}$  and  $\sigma = 0.75$  is used. The grid refinement effect on the jet flow could be reduced if the averaging and diffusion are increased but the intended disturbance would be suppressed.

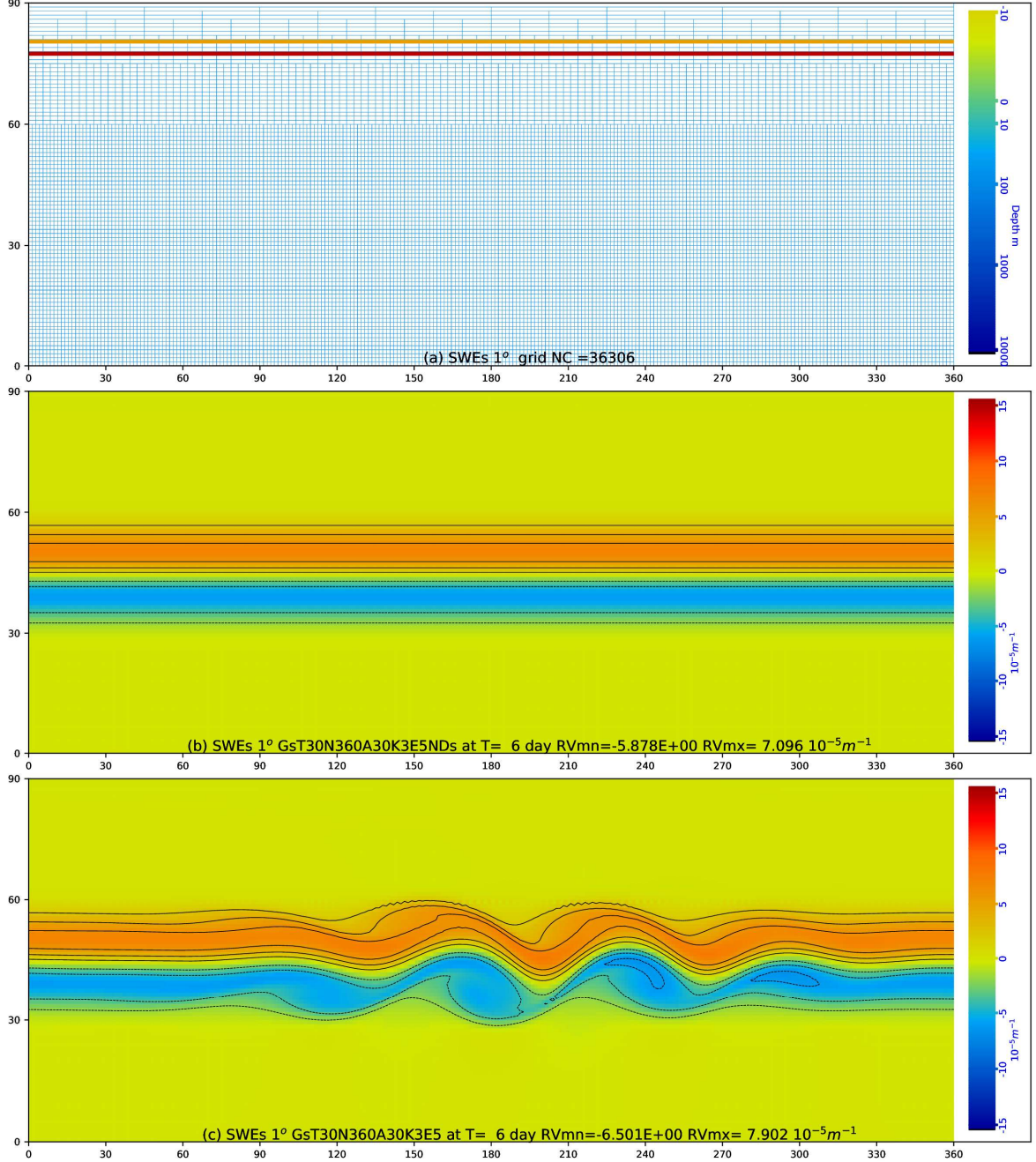


Fig.8 SWEs  $1^\circ$  grid (a) and the relative vorticity after 6 days (b) without and (c) including the initial disturbance in the zonal jet test.

To pinpoint the cause of the vorticity field changes in Fig.7(b) to be the grid refinement, the single resolution SWEs  $1^\circ$  grid is used for this test. The SWEs  $1^\circ$  grid is the same as the SMC  $1^\circ$ MR3 grid except that the refined area is replaced with single resolution cells. Note the SWEs  $1^\circ$  grid is slightly different from the SMC  $1^\circ$  grid used in the previous chapter for transport tests. The SWEs  $1^\circ$  grid has shifted the Equator to be on cell edges so that Coriolis force term at cell centre would not have the singularity on the Equator. Results of the zonal jet test on the SWEs  $1^\circ$  grid are shown in Fig.8. The panel (a) shows the northern hemisphere of the SWEs  $1^\circ$  grid without any refinement. Time step is increased to 30 s as the refined cells are removed. The diffusion and average are kept the same as in value. Taking account the doubled time step, the average interval is increased 2 times as in SMC  $1^\circ$ MR3 test or at every 3 model hours. The panel (b) in Fig.8 shows the model simulated relative vorticity field after 6 model days without the intended initial disturbance. In this case the jet field is maintained steady though slightly weakened by the model numerical dissipation. This confirms that the vorticity field changes shown by the panel

(b) in Fig.7 are caused by the grid refinement in SMC1°MR3 grid. Panel (c) in Fig.8 shows the model relative vorticity field after 6 model days on the SWEs 1° grid when the initial disturbance is included. The wave pattern is like the original one of Fig.6 in Galewsky et al (2004) with explicit diffusion terms because the weighted averaging in this model is like an explicit diffusion term. Contour lines at increment of  $2 \times 10^{-5} \text{ s}^{-1}$ , starting from  $-1.2 \times 10^{-4} \text{ s}^{-1}$ , same as in Galewsky et al (2004), are used for comparison purposes.

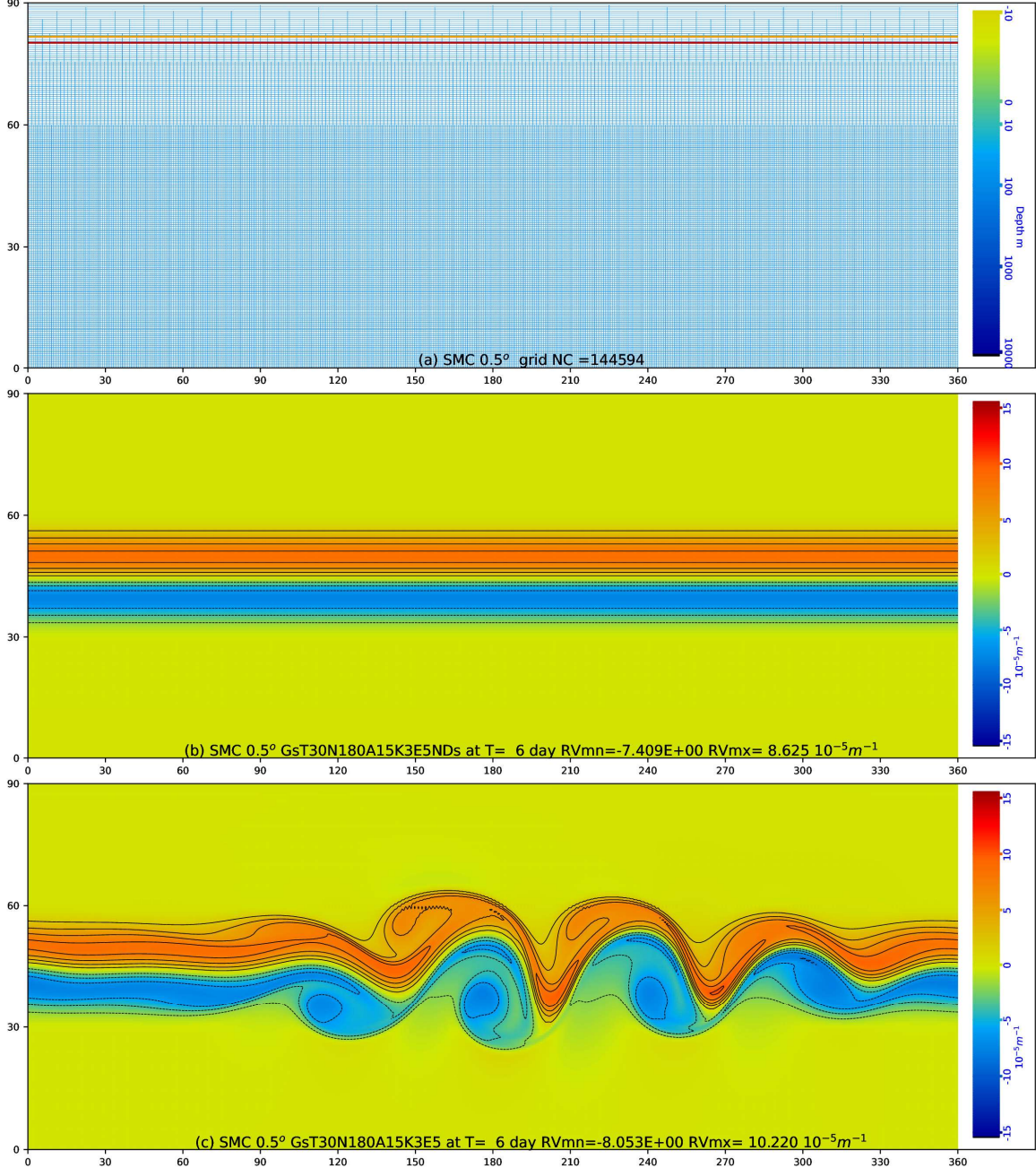


Fig.9 SMC 0.5° grid (a) and the modelled relative vorticity field after 6 days in the Galewsky jet test (b) without (c) with initial disturbance.

Increased resolution will reveal more details of the intended disturbance in the strong jet flow. This is confirmed by the same test on a half-degree single-resolution SMC 0.5° grid and the result is shown in Fig.9. Time step is kept 30 s as in SWEs 1° grid test and global averaging is done every 180 steps or every 1.5 hr model time. Ten extra partial polar averages are added between two global averages or at every 15 timesteps. The thickness diffusivity and polar bias are kept unchanged,  $\kappa_m = 3.0 \times 10^5 \text{ m}^2 \text{s}^{-1}$  and  $\sigma = 0.75$ . The top panel in Fig.9 shows the north hemisphere of the half-degree grid and the middle and lower panels show the model simulated relative vorticity fields after 6 model days without or with the intended initial disturbance. The strong jet is stable if the initial disturbance is excluded as in the SWEs 1° grid case but the SMC 0.5° grid maintains the zonal jet

better than the  $1^\circ$  grid resolution as indicated by the increased vorticity range ( $-7.4$  to  $8.6 \times 10^{-5} \text{ s}^{-1}$ ). The vorticity range in Fig.8(b) for the SWEs 1o grid is from  $-5.9$  to  $7.1 \times 10^{-5} \text{ s}^{-1}$ . The disturbed vorticity pattern in Fig.9(c) is close to the high resolution one of the original Fig.4 in Galewsky et al (2004) and better than the one with explicit diffusion terms in Fig.6 of Galewsky et al (2004). The contour lines are at increment of  $2 \times 10^{-5} \text{ s}^{-1}$ , starting from  $-1.2 \times 10^{-4} \text{ s}^{-1}$ , same as in Galewsky et al (2004). The background colour is, however, drawn cell by cell with 254 colour levels between  $\pm 1.51 \times 10^{-4} \text{ s}^{-1}$ . Note the relative vorticity in the linking area at about  $79^\circ\text{N}$  is also smooth though a different reference direction is used in the polar region, implying that the switch from local east system to the map-east system via the linking zone is smooth.

#### 4. Filling the Mediterranean Sea test

Flooding a low area is a common phenomenon in real life and the process and final state are well known to us. A filling experiment is set up here to test whether the SWEs model could simulate the process of water flowing into low areas and reach a final flat surface state when water sources are exhausted. A 4-level grid of the Mediterranean Sea, as shown in Fig.10, will be used for the filling test of the SWEs model on a regional SMC grid. The grid has a base resolution of 25 km and 3 refined levels at approximately 12, 6 and 3 km and will be referred to as the Medi36125 grid. It cuts off other seas at the Strait of Gibraltar, the Suez Canal and the Istanbul Channel. The latitude and longitude grid lengths at the finest resolution or for size-1 cells are  $\Delta\varphi = 0.029296875^\circ$  and  $\Delta\lambda = 0.0439453125^\circ$ , respectively, which are roughly 3 km in the Mediterranean Sea. The longitude increment is chosen so that merged cells at high latitudes are exact multiples of size-8 cells. As the finest resolution being about 3 km, narrow passes especially those around the Greek Islands are expanded to link up all sea surfaces. This is necessary for the following test because isolated sea basins could not be filled up. The cell floor bathymetric depth at each cell is indicated by its edge colour and the deepest cell is 4632 m from the sea level.

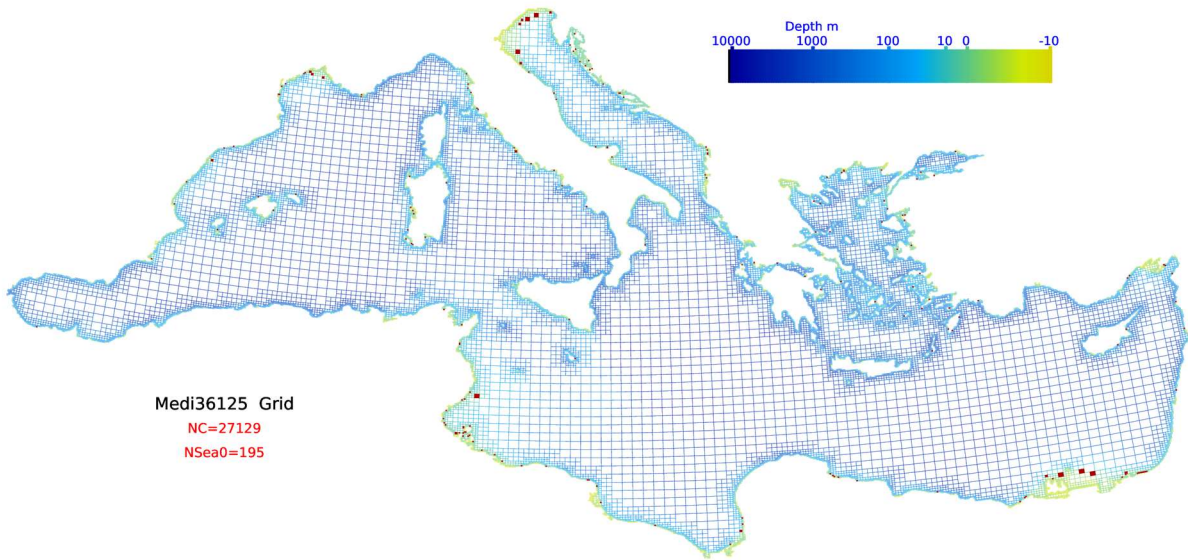


Fig.10 The Mediterranean Sea Medi36125 grid.

The bathymetric depth is an integer in unit of a metre to keep the cell array to be an integer array. If higher bathymetric resolution is required, another unit like centimetre may be used. Apart from the Mediterranean Sea surface area, the Medi36125 grid also covers coastal area up to 10 m above sea level to allow surge inundations. The one metre vertical resolution for the cell floor bathymetry is proportional to the horizontal resolution at 3 km, which is enough for ocean surface wave models but is deemed too coarse for coastal flooding or storm surge. It will be demonstrated later that small surges could be limited by the one metre “walls” if they are not large enough to overcome the one-metre-high steps. Those cells with bottom floor aligned at the sea level will be more likely to be flooded by small surge waves than other coastal cells above the sea level by 1 m or more. The filled red cells in Fig.10 mark those cells with bathymetric floor at the sea level. There are 195 cells whose bathymetric floor are at the sea level, including 3 size-4 cells at the north end of the Adriatic Sea near Venice and 3 in the Nile Delta near Cairo. These two areas will be used to show coastal surges. There are 27,129 cells in total, including 16232, 6459, 2601, and 1837 cells in size 1, 2, 4 and 8, respectively. Note that the finest size-1 cells are more than the sum of all other sized ones. Nevertheless, the multi-resolution grid is still much smaller than a uniform grid at

size-1 resolution, which would have as many as 201,252 size-1 cells or could be more than 7 times as large as the present Medi36125 grid. This reduction on total cell numbers will be significant when high resolution is required for some specific regions.

All the Mediterranean Sea basins are emptied at the start except for a few source cells near river mouths and in strait channels. Water heights in those source cells are maintained at the sea level throughout the experiment to provide unlimited water sources. Water from these source cells will flow into low areas under the gravity force, forming rapid streams or even water falls at the early stage. The water flow will gradually slow down when the water level approaches the sea level and finally stop if the Mediterranean Sea basins are filled up to the sea level because the pressure gradients between the source cells and their neighboring cells disappeared. It is expected that the initial water velocity may be quite large, particularly in areas where the basin floors are steep. In fact, floor level differences between neighbouring cells in the Medi36125 grid may exceed hundreds of metres and initial flows across these cells will be vertical falls higher than any water falls in the world. To prevent the model from crashing out at the early stage due to possible very large flow speed, a speed limit of  $20 \text{ m s}^{-1}$  is applied on each velocity component, which allows a reasonable time step to be used for the whole filling experiment. A 30 s time step is used in this experiment and the maximum diffusivity is set to  $\kappa_m = 3.0 \times 10^5 \text{ m}^2 \text{s}^{-1}$ . Because the Mediterranean Sea is at low latitudes there is no need to change the default parameters for the polar regions.

Panel (a) in Fig.11 shows the initial state of the model and water heights at those source cells are shown by the colour filled cells. Most of the source cell water columns are below 100 m as they are close to river mouths but there are a few over hundreds of metres (highest 742 m), particularly in the Strait of Gibraltar. Panel (b) in Fig.11 shows the water depth after 24-hr filling. The waters from the Strait of Gibraltar and River Rhone, south of France, first pool in the basin to the east of Spain. The water from Venice flows a long way through the Adriatic Sea and pools in the Ionian Sea basin. Rivers Vardar and Struma in north Greece feed directly into the Aegean Sea. The source water from the Black Sea via the Istanbul Channel pools in the Sea of Marmara first and then spills over a narrow channel into the Aegean Sea. The water from the River Nile Delta feeds directly into the main basin in the east of the Mediterranean Sea. Note the flow from the River Nile is not presented as continuous in the shallow area in panel (b). This is because the positive filter for water height has thrown out some negative water heights and reset them to be zero. Because of the rapid flow speed in this area due to the steep gradient, the model advection scheme may have created some minor oscillations there.

Panel (c) in Fig.11 shows the simulated water depth after 10-day filling. By this time water pooled in the west basin has spilled over the underwater ridge between Sardinia and Tunisia into the Tyrrhenian Sea, to the west of Italy. Flooding waters from Adriatic Sea, Aegean Sea, and Rive Nile delta have met in the east and central basin of the Mediterranean Sea, forming the largest basin pool so far. Panel (d) in Fig.11 is the water depth after 20 days. By then waters from all sources have linked up after the Tyrrhenian Sea and Ionian Sea are linked up, left only some shallow coastal patches to be dry. Panel (e) in Fig.11 is the water depth after 40 days filling and by this time the whole Mediterranean Sea is already filled up. This is indicated by the maximum depth of 4632 m. The unflooded areas, particular in Venice and the River Nile delta, are above the sea level. The final plot of Fig.11 is the water depth after 100 days, which is almost identical to panel (e) of the 40 days plot. This confirms that the model stayed stable after the Mediterranean Sea is filled up.

The filling process may also be illustrated by the flow speed plots in Fig.10.3. Panel (a) in Fig.12 shows the modelled flow speed after 10 days. Water speeds close to source points are almost at the maximum speed as indicated by the red-coloured cells. Remember the model has a velocity component limit of  $20 \text{ m s}^{-1}$  so the maximum speed is  $28.28 \text{ m s}^{-1}$  as indicated in the plot. To avoid output underflow in the scientific notation, small velocity components of absolute values below  $1.0 \times 10^{-90} \text{ m s}^{-1}$  are all saved as  $1.0\text{E}-90$ . Hence the minimum speed of  $1.414\text{E}-90 \text{ m s}^{-1}$  should be treated as zero speed. Only the water flow out of the Istanbul Channel has almost stopped because the small Sea of Marmara is nearly blocked by the narrow channel linking the Aegean Sea. Water is still flowing through the channel but very slowly. The broken flow off the River Nile delta reveals the large speed gradient there. In fact, they are water falls due to the sharp fall of the basin floor beyond the Nile delta.

Panel (b) in Fig.12 shows the water speed after 20 days. Apart from the high speed near water sources, the spilling flow from the Tyrrhenian Sea to the Ionian Sea is also quite rapid. This is because the water source from the Strait of Gibraltar is much stronger than other sources and the west basins are filled up more quickly than the central and east basins. Broken flow off the Nile delta due to transport oscillation is still present after 20 days. Panel (c) in Fig.12 shows the water speed after 40 days. By this time the filling has already completed so the maximum speed dropped to  $0.14 \text{ m s}^{-1}$ . This is probably an oscillation speed caused by gravity waves as small maximum speed around this order is maintained until the end of the model run of 200 days. Water flows have stopped by 40 days, but gravity waves may linger a bit longer.

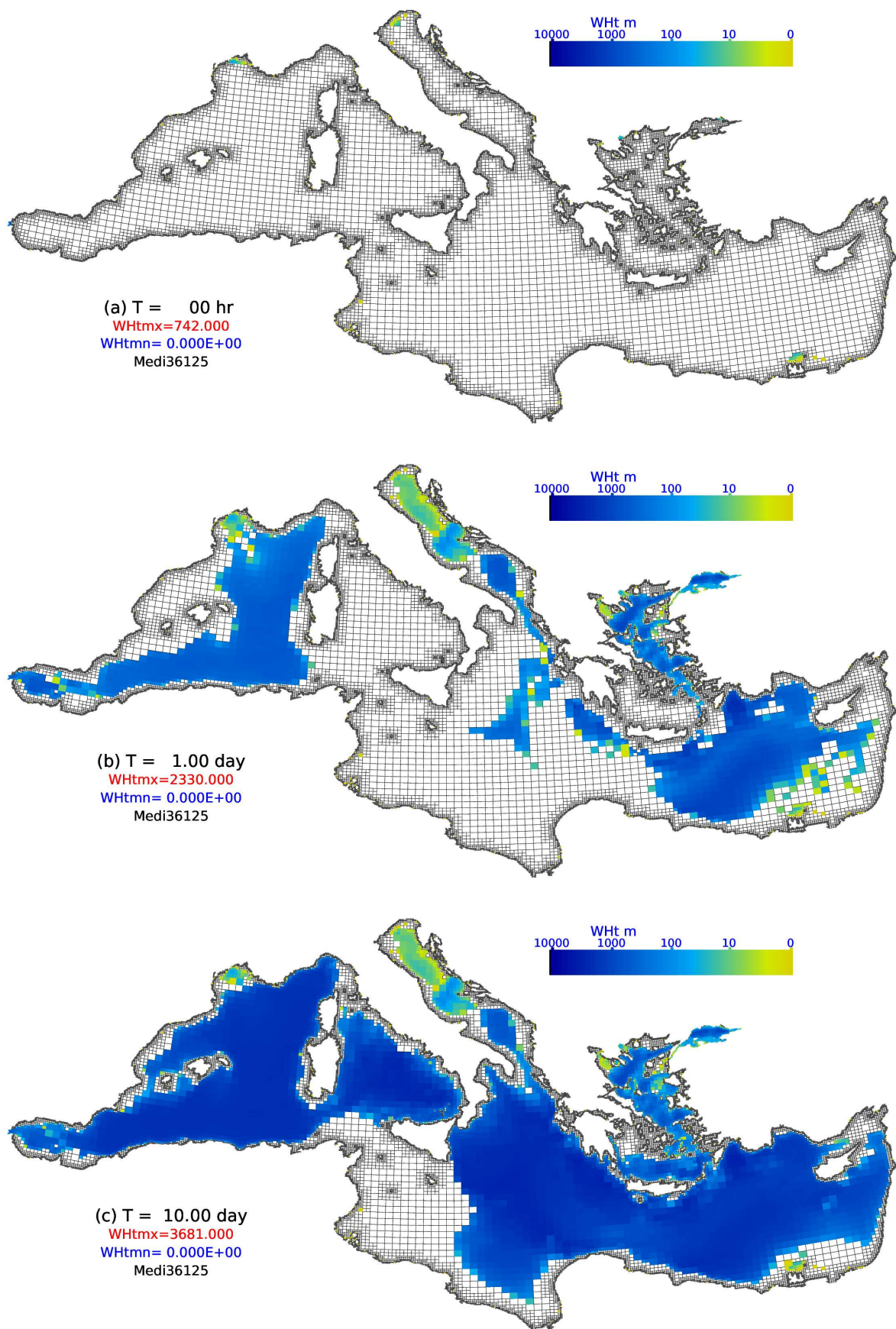


Fig.11(a-c) Filling the Mediterranean basins with constant river sources (a) and the simulated flooding after 1 (b) and 10 days (c).

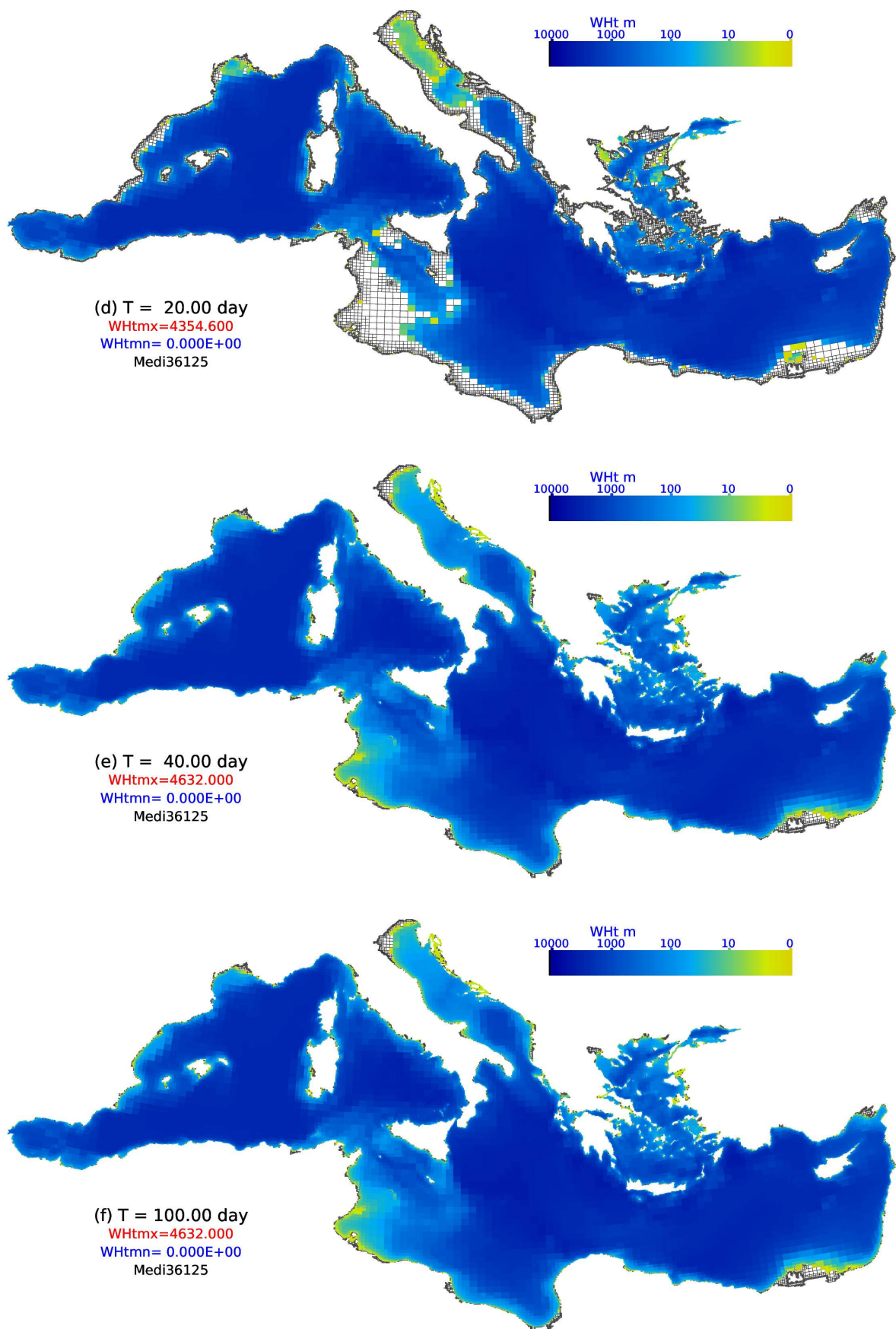


Fig.11(d-f) Simulated filling of the Mediterranean Sea after 20 (d), 40 (e), and 100 days (f).

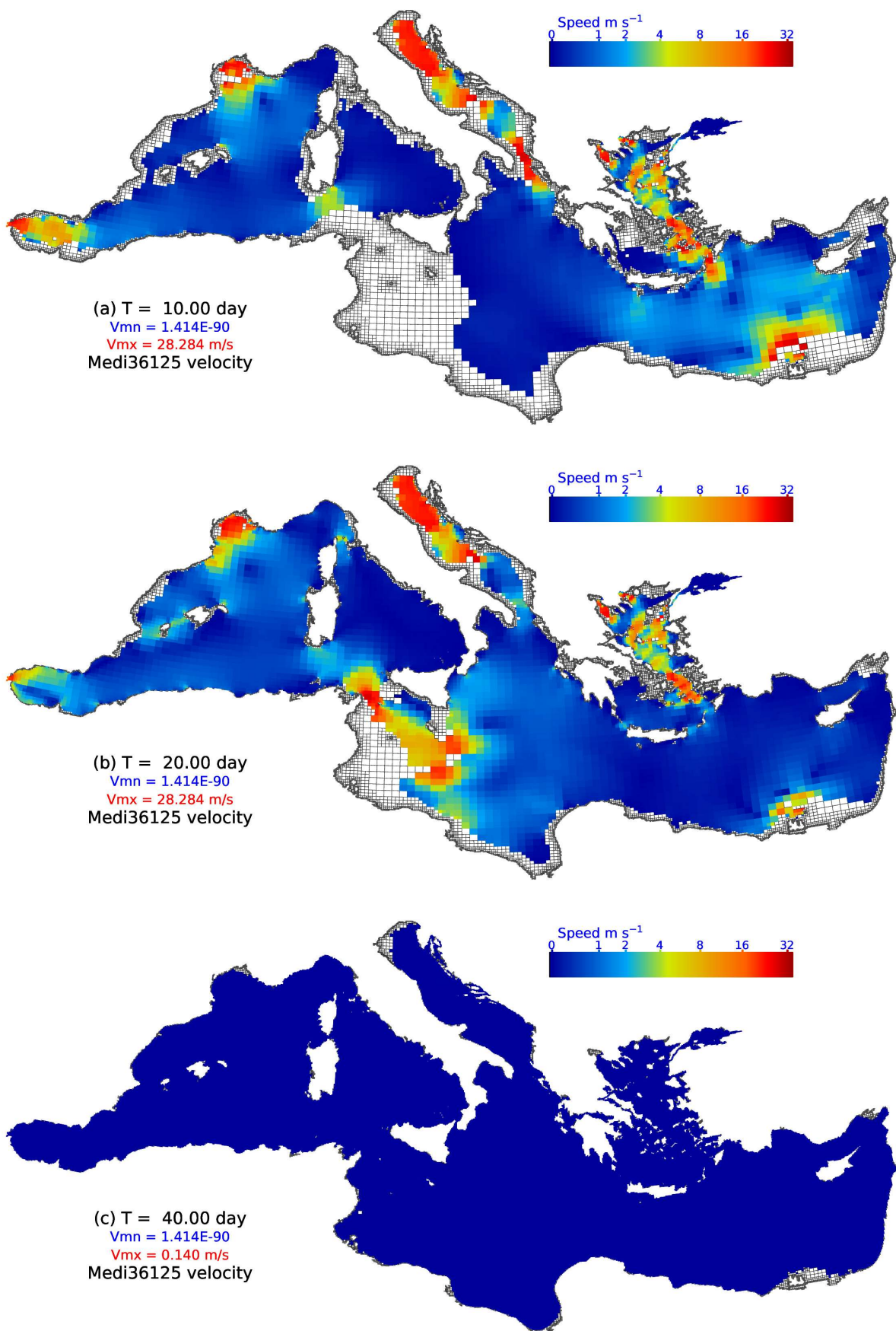


Fig.12 Flow speed in the filling test after 10, 20 and 40 days.

To estimate the filling rate, the water volume in the Mediterranean basins during the filling test is integrated at regular intervals and is shown in Fig.13. Water volume in each cell is measured by its floor area in steradian at the Earth's radius, multiplied by its water column height in metre, so the total water volume is given in the unit of m sr. Taking the Earth's radius as 6371 km, 1 m sr is about  $40590 \text{ km}^3$ . The initial water volume is not zero because of the source cells are filled up to the sea level during the whole test. The initial volume is about  $3.2\text{E}-3 \text{ m sr}$ . The filling rate is largest at the start and almost a constant during the first few days. This is because the water flow speed is limited by the maximum velocity component of  $20 \text{ m s}^{-1}$ . After the initial rush the filling rate slows down due to the decrease of water level differences between the source cells and their neighbouring cells. After about a month, all the basins are almost filled up and the filling rate eventually becomes zero when the whole Mediterranean Sea is filled up to the sea level. The total water volume remains constant afterwards to the end of 200 model days but only the first 50 days are shown here. The total volume of the Mediterranean basins up to the sea level is about 94.0 m sr as represented by the Medi36125 grid.

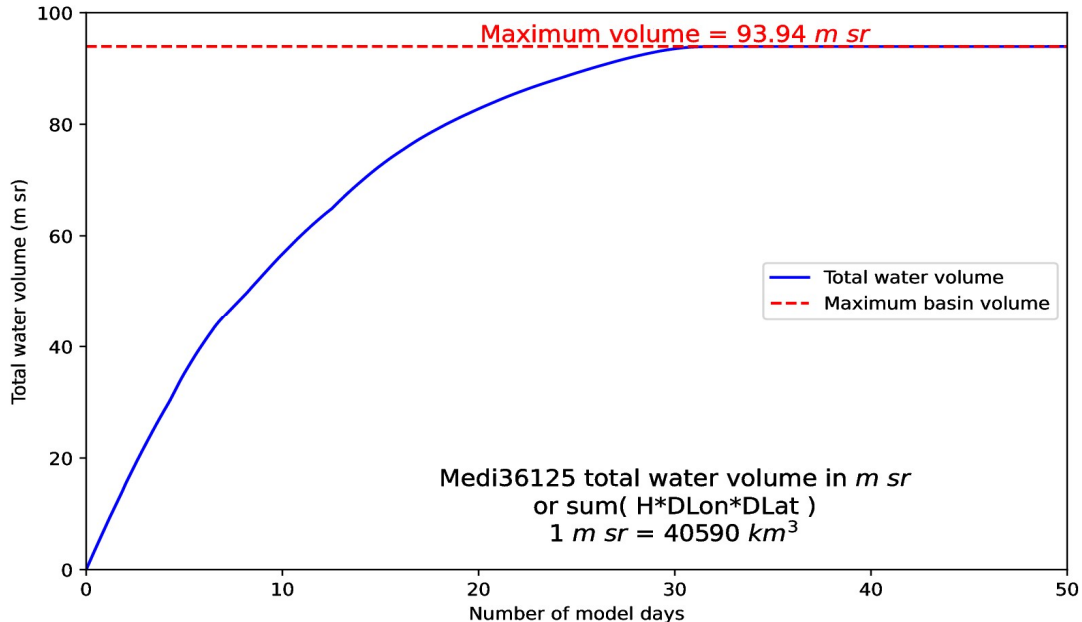


Fig.13 Time series of total water volume during the filling test.

Although we could not do this experiment in the real world, the filling processes presented here agree well with our expectation. The experiment has demonstrated that the dry-wet change over the whole sea area goes well, and it is reasonable to expect that it will perform well in coastal regions. The simulated final flat Mediterranean Sea agrees with our expected “lake at rest” as there is not any disturbing force in the model. If an initial disturbance is introduced, gravity or tsunami waves could be stirred up.

## 5. Tsunami waves in the Mediterranean Sea

Shallow water equations (SWEs) have been used widely for tests of numerical algorithms and different model grids as discussed in previous sections because they are a simple set of 2-D fluid dynamical equations. SWEs also have many real applications, such as numerical modelling of ocean storm surges and tsunami propagations. For instance, the SLOSH surge forecasting model (Glahn et al., 2009) and GeoClaw tsunami model (Berger et al. 2011) are based on the SWEs. Routine surge forecasting is part of coastal hazard warning system in most weather forecasting centres over the world and tsunami studies are greatly accelerated after the 2004 Indian Ocean tsunami. Synolakis and Bernard (2006) reviewed the history of tsunami studies before the 2004 Indian Ocean tsunami and emphasised the importance of developing tsunami inundation modelling tools for inundation forecasting and model validations with observations from different instruments.

As tsunami waves usually travel a long distance, both their ocean basin-scale propagation and detailed nearshore inundation need to be simulated. This is a challenge to conventional model grids because limited computing resources prohibit both a large domain and a high-resolution mesh in a single model. A straightforward solution is by using nested grids and an alternative approach is building a multi-resolution grid model. Finite element methods on unstructured triangular cell grids have been successfully applied in surge and tsunami models, such as the application of the ADCIRC surge model (Musinguzi et al., 2019) and the SCHISM tsunami current model

(Zhang et al., 2016). An unstructured triangular cell grid provides fine resolution near coastlines and inland waterways along with gradually relaxed coarser resolution cells offshore. However, this paradigm usually requires a lot of computing resources and may not meet the timeliness requirement of surge forecasting and tsunami warning. Adaptive mesh refinement (Berger and Oliger, 1984) was originally aimed to get refined resolution of tropical storms within a large coarse grid and it was later adapted in tackling the large-domain and high-resolution conflict with combination of static refinement near coastlines and the normal adaptive refinement (Popinet and Rickard, 2007). LeVeque et al. (2011) demonstrated how finite-volume algorithms are combined with adaptive mesh refinement techniques in simulation of transoceanic tsunami propagation and detailed modelling of inundation in refined coastal regions, using the depth averaged SWEs. Popinet (2011) implemented a well-balanced, positive-preserving scheme of Audusse et al. (2014) for SWEs on a quadtree-adaptive grid to simulate tsunami waves. This quadtree-adaptive grid is also used in ocean surface wave model to gain dynamical refinement of tropical storm source areas (Popinet et al., 2010).

The SWEs model on the SMC grid is a combination of the latitude-longitude grid and unstructured grid technique. It also supports static mesh-refinement so coastal refinement could be achieved for resolving small islands and modelling coastal inundations. The experiment of filling the whole Mediterranean Sea has demonstrated that the model could simulate the water pooling in expected process and reach the final flat surface state. This section will simulate the propagation and dissipation of an initial disturbance on a flat sea surface or possible tsunami scenario in the Mediterranean Sea.

The time step and diffusion coefficient are set the same as used in the previous filling experiment. The whole Mediterranean Sea is assumed to be at rest with a flat surface at the sea level, except for 4 size-8 cells to the east of the Sicily Island in the Ionian Sea. A 5 m high water column is taken from 2 cells and added to its neighbouring 2 cells, forming an initial disturbance of  $\pm 5$  m shift of the water surface as shown by the water height difference from the sea level in panel (a) of Fig.14. The four disturbed size-8 cells cover an area about  $60 \times 50 \text{ km}^2$ , close to an area hit by a moderate earthquake. The  $\pm 5$  m initial disturbance is of the same order as the 2004 Indian Ocean earthquake as estimated by Pietrzak et al. (2007) though the disturbed area is much smaller than the 2004 one. The model is then let free to run until its flat surface is restored. It is envisaged that gravity or tsunami waves may be generated by this initial water surface shift. Panel (b) in Fig.14 shows the water height difference from the sea level after 1 h model time. Gravity waves of magnitude about 7 cm are visible within about 600 km from the initial disturbance site. As the water depth in the Ionian Sea is about 3000 m and the tsunami waves speed is approximately  $\sqrt{gh} \approx 170 \text{ m s}^{-1}$  in the Ionian Sea. The tsunami wave at this speed covers roughly 600 km in one hour. There are two wave crescent circles, so the gravity wavelength is about 300 km, which is a typical tsunami wavelength in open oceans where the water is over thousands of metres deep.

Panel (c) in Fig.14 is the water height difference after 4 h model time. By then the tsunami waves have reached the coastlines of the whole Mediterranean Sea. Because the distance from the Strait of Gibraltar to the Nile River delta spans over  $36^\circ$  longitude at the latitude of  $35^\circ\text{N}$  the Mediterranean basin size from west to east could be estimated to be  $(\pi r/5)\cos 35^\circ$  or about 3300 km, which could be covered by the tsunami in about 5 hr. The maximum magnitudes of the tsunami waves have fallen below 1 cm after 4 hr and it must be at centimetre order at coastlines. These small tsunami surges are hardly visible by naked eyes and only manifest themselves in those cells with bottom floor at exactly the sea level. To show this small surge effect, those cells at sea level are marked dark red when they are dry in Fig.14. At the start in panel (a) or the  $T = 0$  plot all the cells at the sea-level are dry and the marked cells in dark red are the same as in the Medi36125 grid shown in Fig.10. In panel (b) of Fig.14 at  $T = 1$  hr, the first tsunami surge just reached the south Adriatic Sea and flooded a few sea-level cells there. The Venice coastal area remains intact, and those sea-level cells are still at its initial dry state, indicated by the red colour. The first wave arrives at the Venice coast in about 3 hr and maintains the surge for another 3 hr there while the first wave crescent comes and returns. The panel (c) of Fig.14 at  $T = 4$  hr shows that the surge has inundated almost all the sea-level cells in the Mediterranean Sea though the water height is not significant (maximum surge height about 1 cm). The small surge could not overcome the cliff walls (at least 1 m high above sea level) beyond the sea level cells and is reflected into the sea.

Another initial disturbance rotated by  $90^\circ$  from that in the previous experiment is used to illustrate the directional effect of the initial disturbance. Panel (a) in Fig.15 shows the rotated initial disturbance which is now with a 5 m dip on the west and a 5 m lump on the east side. Panel (b) in Fig.15 shows the water height difference from the sea level after 1 hr model time. The maximum wave height difference is now about 16 cm, more than doubled that of the previous test. Also note the tsunami waves travelling towards the west has a recession or trough in the front instead of a crescent surge in the first experiment. The east travelling waves also reversed to a surge in the front from the recession in previous test. The wavelength looks close to that of the first experiment because it is determined by the underlying bathymetry. Tsunami waves in the Ionian Sea travel faster than in the Adriatic Sea because of the Ionian Sea is much deeper than the Adriatic Sea.

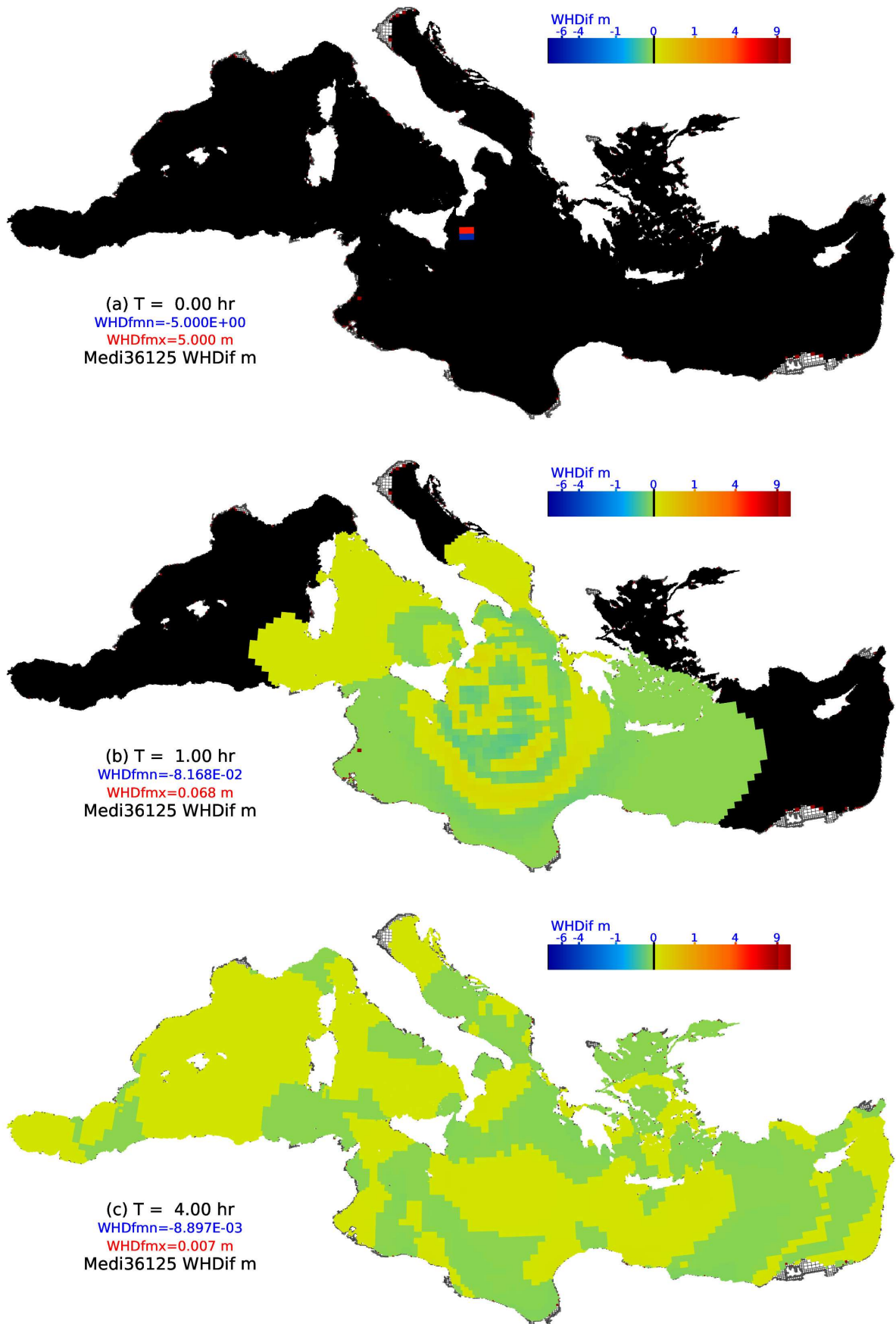


Fig.14 Simulated tsunami waves in the Mediterranean Sea with idealized initial disturbance in the Ionian Sea.

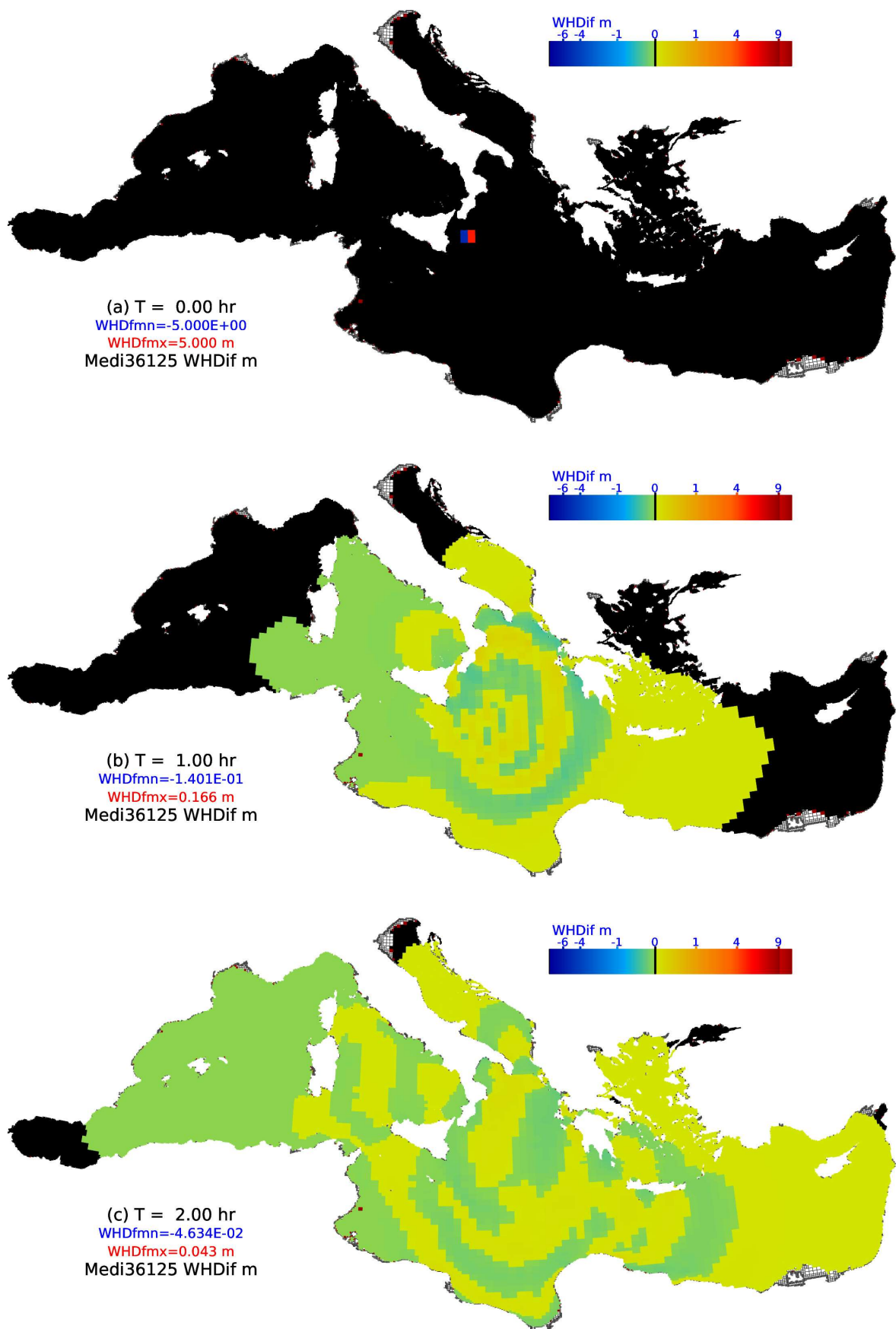


Fig.15 Same as Fig.14 but with an initial disturbance rotated by  $90^\circ$ .

The first wave arrives at the Nile Delta in about 1.5 hr and maintains the surge there over an hour. Panel (c) in Fig.15 shows the water height difference after 2 hr model time when the first wave surge is travelling through the Nile River delta area. The maximum surge is about 4 cm, which is higher than that of the first experiment but is still very small in comparison with normal tidal waves. Nevertheless, the surge has turned the initial dry sea-level cells in the Nile River delta area into wet cells, which could be seen by comparing panel (c) with (b) in Fig.15 though their water height differences are quite small. The differences between the two tests indicate that the orientation of the initial disturbance has visible influences on the subsequent tsunami waves, apart from the intensity of the initial disturbance. This test indicates that the SWEs model is capable of modelling tsunami waves though the coastal surge may be underestimated.

## 6. Simulations of the 2004 Indian Ocean tsunami

The 2004 Indian Ocean tsunami was perhaps the most devastating tsunami in recorded history, causing over 200,000 fatalities and widespread destruction in and beyond the Indian Ocean (Grilli et al, 2007). It was generated by an earthquake of moment magnitude about 9.2, occurred at 0059 UTC on 26 December 2004 in the Bay of Bengal. It was a truly global event with many measurements made with seismometers, tide gauges, global positioning system stations, and a few satellite overpasses around the world. For this reason, a global SMC grid is created for the SWEs model to simulate this tsunami case.

The SMC grid used for this global tsunami model consists of cells of multiple size-1 latitude increment of  $\Delta\phi=0.025^\circ$  and longitude increment of  $\Delta\lambda = 0.03515625^\circ$ . The longitude increment is chosen so that a full parallel circle around the earth is exactly 10240 or  $5 \times 2^{11}$  times of the size-1 longitude grid length, which makes it easy to merge cells at high latitudes. The grid size-1 cell is about 2.5 km in both directions at mid-latitudes and all coastlines in this global grid are resolved at the size-1 resolution. The cell sizes increase gradually with distance from coastlines by doubling the size-1 lengths in both directions until the spatial resolution for open ocean surface reaches the size-8 base resolution or  $0.2^\circ \times 0.28125^\circ$  in latitude-longitude degrees, which is approximately 20 km at mid-latitudes. The grid is then referred to as a 4-level (2.5-5-10-20 km) SMC global grid or SMC251020 grid as shown in Fig.16. The numbered marks indicate selected sites of runup observations for the 2004 Indian Ocean tsunami, compiled by National Geophysical Data Center / World Data Service (NGDC/WDS). The Black Sea, Caspian Sea, and the Great Lakes have been removed from the grid as they are not linked to the open oceans. Other inland water surfaces and lowlands are also trimmed away because they are unlikely to be affected by ocean tsunamis.

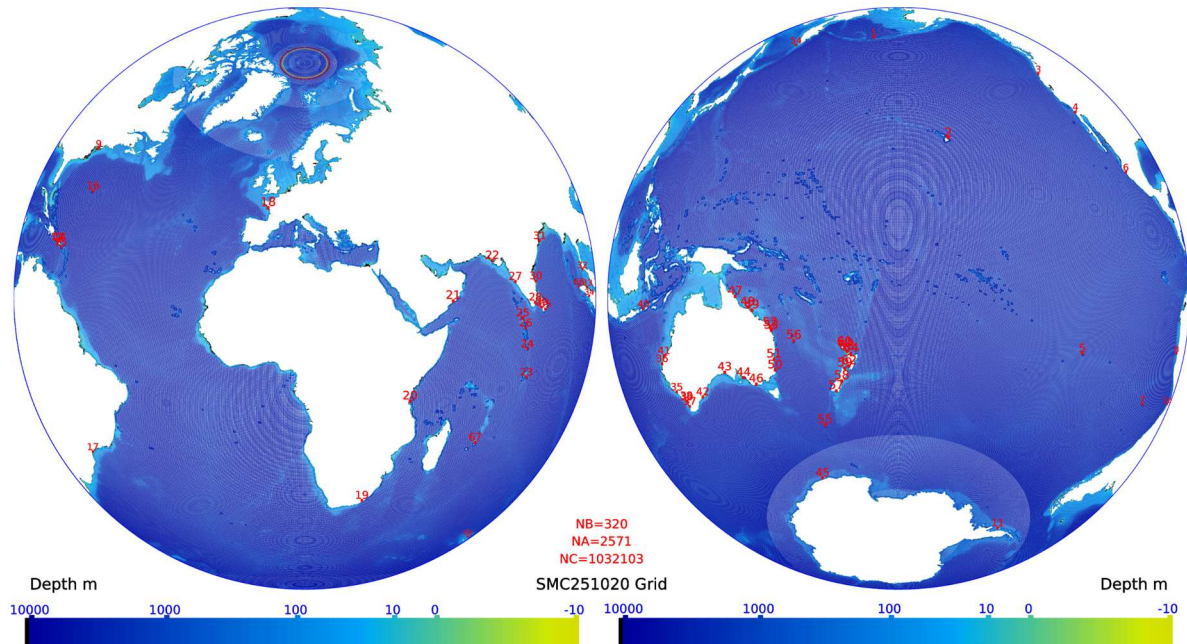


Fig.16 The SMC251020 global tsunami model grid.

Apart from the ocean surface area, the grid is extended to cover coastal land area up to 10 m above sea level to simulate possible tsunami inundation. The vertical resolution for ocean floor bathymetry is rounded to an integer

in metre, which is proportional to the horizontal resolution at 2.5 km and fit for simulation of tsunami wave propagation in the open oceans. If higher bathymetric resolution is required, another unit like centimetre may be used. The vertical resolution of 1 m and horizontal resolution of 2.5 km at coastal area are, however, deemed too coarse for coastal tsunami runup. For this preliminary global tsunami model, the main target is to get a global view of tsunami propagation rather than detailed runup at coastal and inland areas, which may require spatial resolution down to tens of metres.

There are just over 1 million cells in this global grid (1,032,103), including 164005, 189193, 81123, and 597782 cells at size 1, 2, 4 and 8, respectively. Note that the total number of cells is still smaller than a normal regular latitude-longitude grid at the same 20 km base resolution (1280x900 = 1,152,000) despite of the increased resolution to 2.5 km at coastal areas. This is because the unstructured SMC grid cells does not need to cover any inland areas except for flooding zones. Trimmings of the inland water surfaces and lowlands have also removed over 70 thousand cells and the multi-resolution allows over half of the total 1 million cells to be at the base resolution of 20 km. This reduction of total number of cells and the relaxed timestep with merged cells at high latitudes ensure that the SMC grid model is faster than a regular grid model at the same 20 km base resolution. A regular grid at the size-1 resolution (10240x7200 = 73,728,000) would be over 70 times larger than this multi-resolution grid and will need a supercomputer to run rather than a desktop machine used for this study.

The diffusion coefficient is a key parameter which has strong influence on the model's stability and performance. It should be large enough to suppress the 2-grid numerical oscillations and some false short waves, which may spoil the model performance if their growth is unchecked. If the diffusion is too strong, however, it may smooth out real oscillations as well. On the other hand, it is required to ensure the Fourier number to be less than  $\frac{1}{2}$  for model stability. For this global tsunami model a maximum diffusivity of  $\kappa_m$  is chosen to be just enough to suppress the numerical oscillations. As the numerical oscillation strength is accumulated during the model run, a ramping factor with time is introduced for the diffusion coefficient to increase with model time, and it becomes

$$\kappa = \kappa_m(1 - \gamma + \gamma \sin^2 \varphi)(1 - \sigma e^{-t/\tau}), \quad 0 \leq \gamma < 1, \quad 0 \leq \sigma < 1$$

where  $\gamma$  is the polar bias factor,  $\varphi$  the latitude,  $\sigma$  is the complementary initial ratio,  $t$  the model time and  $\tau$  the ramping time at which the diffusivity reaches  $1-\sigma/e$  times of the maximum value. This ramping increase of the diffusion coefficient allows the tsunami waves to be less smoothed at the early stage and the diffusion to be enough for suppressing the numerical oscillations with increasing model time.

Initialization of earthquake disturbance in sea water is regarded as the first critical stage in the simulation of the whole lifecycle of tsunami. Its implementation is conventionally based on the assumption that the initial sea surface condition is identical to the vertical displacement at seafloor due to fault rupture. The vertical deformation is generally assumed to be instantaneous, on the basis that the phase velocity of a tsunami is much slower than the propagation velocity of earthquake rupture. The static seafloor deformation is calculated with the Okada (1985, 1992) formulas (<https://github.com/hydrocoast/>), which is used for a few tsunami models, such as Grilli et al. (2007), who developed a tsunami source made of five properly parameterized dislocations sources for the 26 December 2004 Indian Ocean tsunami. Following Grilli et al. (2007) source model the initial seafloor deformation is transformed into an equivalent initial water surface disturbance for each SMC grid cell within the source area for initialization of the tsunami simulation. Initial momentum of sea water caused by the earthquake is not considered for this preliminary study.

A 30 s time step is used in this global SWEs model, and the maximum diffusivity  $\kappa_m$  is set to be 4.0E5 m<sup>2</sup> s<sup>-1</sup> for the continuity equation with a polar bias factor  $\gamma = 0.1$ , the complementary initial ratio  $\sigma = 0.8$  and the ramping time  $\tau = 12$  hr. The diffusion coefficient is smaller than the possible maximum value allowed on this grid, which is about 6.0E5 m<sup>2</sup> s<sup>-1</sup> by the Fourier number stability restriction. A 1-2-1 weighted average is applied to the horizontal velocity field at every 10 timesteps or 5 minutes model time, which is an optimised interval just enough for suppressing the instability in the momentum equations. The bottom friction coefficient is set to be 0.0015 as discussed in the previous chapter. The model run started with the initial earthquake disturbances and ran for 50 hrs, which is roughly the time required for the tsunami waves to cover the full globe distance. Outputs of water height difference (WHDif) from the sea level at the 68 selected runup observation sites are saved every minute while full grid WHDif is saved at varied intervals from 15 min at early model hours to 2 hr towards the end of 50 hr model run.

Fig.17 shows the water height differences of the simulated Indian Ocean tsunami at 3 model times. The top panel is the initial water height differences at the start of the model run. It covers the Indian Ocean earthquake area from about 88° to 98° in longitudes and from -2° to 16° in latitudes, with a horizontal resolution of 1 arcmin or about 1.8 km in both directions. The initial disturbance range is from about 4 m below the sea level to about 7 m above it, which is very close to the estimated one by Pietrzak et al (2007), using GPS analysis of fault line slip.

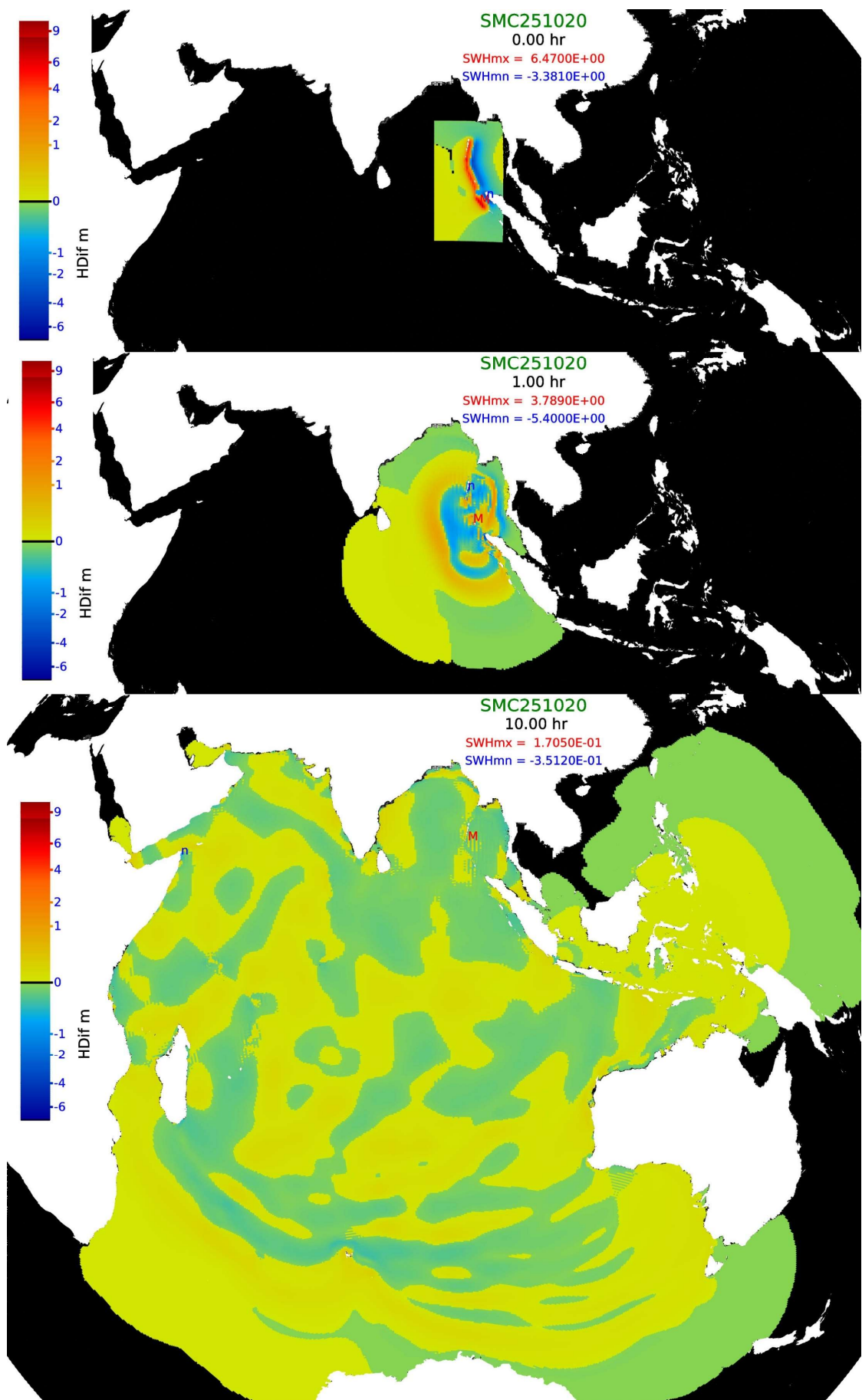


Fig.17 Simulated 2004 Indian Ocean tsunami at 0, 1, and 10 hrs.

The initial water height disturbances are averaged within each cell area at varied resolution of 2.5, 5, 10 and 20 km resolutions and the shift range are slightly reduced from the original disturbance as shown in the top panel (-3.38 to 6.47 m). The cell with the maximum water level lift is marked by the “M” and the one with deepest water level drop by the “n” symbols in the diagram. The middle panel in Fig.17 shows the model simulated tsunami wave field at 1 hr after the earthquake. A ring of high wave has spread out of the earthquake-stricken area with peak height over 3.80 m and trough depth of 5.40 m. Note the minimum depth of the initial disturbance is less than 4 m, the tsunami wave is deepened first, corresponding to the observed early water retreat. The fronts of the tsunami waves match the initial orientation of the earthquake disturbances, that is, the westward waves are leading by a high wave peak while the eastward waves are fronted with a trough, indicating that the shape of the initial disturbance has strong influence on the subsequent tsunami wave pattern. The vertical lines of waves in the source area around the maximum “M” and minimum “n” markers indicate the 2-grid numerical oscillations as the wavelength is exactly 2-cell wide (40 km long). This kind of numerical oscillations could be suppressed by increased diffusion. For instance, the vertical lines disappeared when the diffusion coefficient was increased to  $6.0E5 \text{ m}^2 \text{ s}^{-1}$ . However, the increased diffusion will also smooth down the tsunami waves as well. In this simulation the diffusion is chosen as small as possible so that the numerical oscillations would not grow out of control or spread outwards. If a better way to control the numerical instability could be found without using the strong smoothing scheme, the modelled tsunami wave height could be increased further. Increasing the spatial resolution is one possible approach to reducing the smoothing effect because the required diffusion coefficient to control the 2-grid length oscillation is reduced with reduced grid length.

The numerical oscillation is closely related to local bathymetry. For instance, slightly reducing the floor gradient around an oscillation spot would mitigate the oscillations. The mechanism to stimulate the oscillation needs further investigation. Despite of the effort to minimise the numerical smoothing, the tsunami wave heights are still underestimated by this global model, and it will be discussed in more detail in comparison with observed runups. The lower panel in Fig.17 illustrates the simulated tsunami waves at 10 hr after the earthquake. By that time the tsunami waves have spread all over the Indian Ocean. The tsunami wave magnitude is between -0.35 and 0.17 m. There are still some 2-grid oscillations in the source area, particularly near the maximum wave height marker ‘M’, but the magnitude is much lower than those at 1 hr time (mid-panel). This confirms that the diffusion coefficient is large enough to suppress the spreading of the numerical oscillations, though not large enough to eradicate them. New oscillations may be excited when the tsunami waves spread over new possible oscillation spots, such as those vertical lines appeared off Sri Lanka coast in this 10-hr wave height field.

Fig.18 is the global view of the simulated Indian Ocean tsunami after 1 day (top panel) and at the end of model run, 50 hr after the earthquake (bottom panel). The tsunami wave magnitude is reduced below 0.1 m after 2 model days despite of some localised numerical oscillations as indicated by the overlapping “n” and “M” markers in the final wave height plot. The tsunami wave reached the east Pacific and north Atlantic in about 1 day time and covered the whole global ocean surfaces in 2 days. The remaining black cells along coastlines in the bottom panel are land cells (up to 10 m above the sea level) not flooded by the tsunami waves. This SMC251020 grid SWEs model is designed to show the propagation of tsunami waves over the global ocean surfaces but it is not good enough to simulate the real runup of tsunami waves up coastal land area because of its numerical limitation to describe the real tsunami runup and the coarse resolution of 2.5 km to represent the true coastal bathymetry, particularly river estuaries. Further increase of the horizontal resolution by adding more resolution levels in the SMC grid could improve the coastal wave simulation while increase of the base resolution could improve the overall global tsunami presentation. For example, a 5-level grid with the same coastal resolution of 2.5 km but reduced base resolution of 40 km for open ocean surfaces has been used before this 4-level grid. The tsunami waves are underestimated further than the present 4-level grid with base resolution at 20 km, particularly because of the increased diffusion to control the 2-grid waves in the 40 km base resolution model. It is expected that further increase of the base resolution to 10 km or even 5 km and coastal resolution to tens of metres would greatly enhance the simulated tsunami wave height. However, it would result in a large global model and require a supercomputer to run it. One possible target for future improvement is to use multi-grid SMC grids as suggested in Li (2022) for the WAVEWATCH III model (WW3DG, 2019). This may allow a few of ocean basin sub-grids to be run in parallel or independently and could create room for higher base resolution and coastal refinement. For instance, the Pacific Ocean is more susceptible to tsunamis and can be covered in one sub-grid, which could be run independently by ignoring boundary exchanges with other ocean basins or merged with other sub-grids as a global model for a parallel run if needed.

Fig.19 shows the time series of the propagated tsunami energy in the SMC251020 model for the 2004 Indian Ocean tsunami case at every 6 timesteps or 3 min. Note that the initial earthquake disturbance used in this simulation did not have any momentum input, so the initial kinetic energy is zero. The initial total energy consists of only the potential energy or the initial water surface disturbances. The modelled initial potential energy is about  $7.56E13 \text{ J}$ , which is believed to be lower than the real tsunami energy as another simulation of the 2011 Tohoku Pacific Ocean tsunami underestimated the observed tsunami energy (Li and Wang 2024). One reason is the lack

of initial earthquake momentum input for this simulation. The modelled kinetic energy is zero at start and it jumps up to about the same value as the initial potential energy (7.56E13 J) within the first 6 timesteps. This may imply that initial kinetic energy disturbance by the earthquake should be considered for a better simulation of the tsunami waves. The modelled kinetic and potential energy values are almost equal in the subsequent model times except for some minor fluctuations while the total propagated energy drops steadily with time. This is expected because there is no other energy input to the model except for the initial earthquake disturbance.

Another possible reason for the underestimation of total tsunami energy may be the potential energy reference point at sea-level, which assumes the global ocean water surface is flat at the sea-level. This is, however, not the same as the real-world ocean sea-level point, which includes some geodetic variations. Tsunami wave energy is dissipated by coastal wave energy consumption and the model smoothing, which may also contribute to underestimation of total tsunami wave energy due to the removal of short waves.

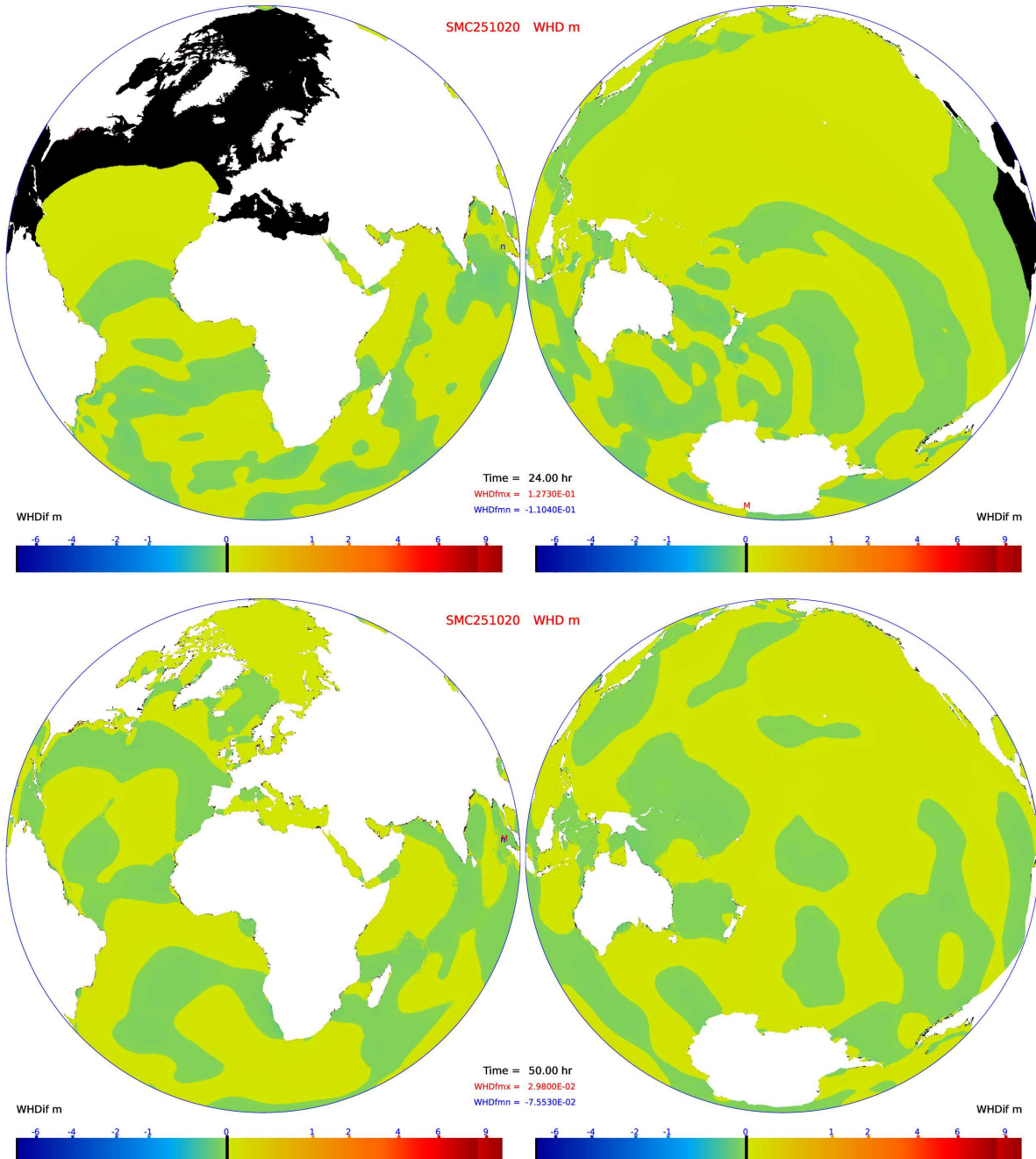


Fig.18 Simulated 2004 Indian Ocean tsunami after 24 and 50 hrs.

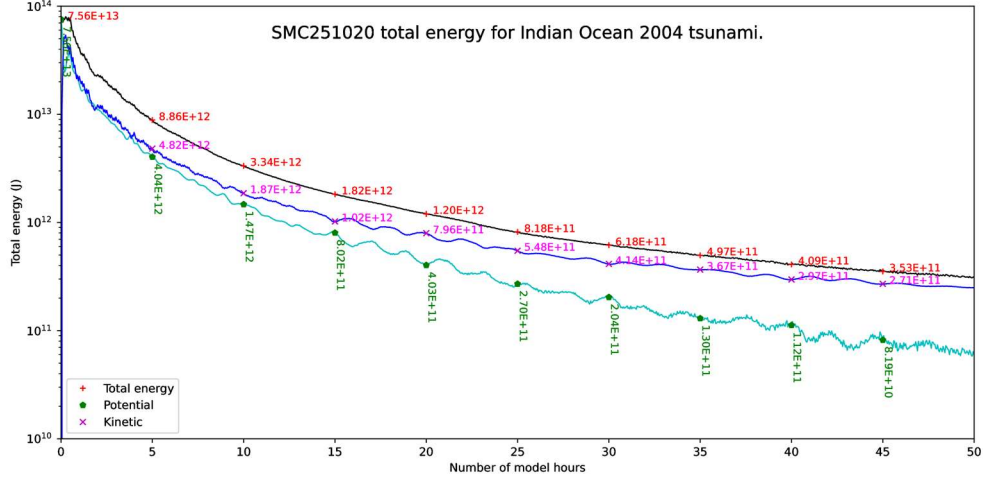


Fig.19 Simulated total energy of tsunami wave in the 2004 Indian Ocean tsunami case.

## 7. Comparison with Indian Ocean tsunami observations

Observations of tsunami waves in the open ocean surfaces are rare because of a few reasons. First is that there are not many observational instruments installed for such global observations. The second reason is that tsunami wave height is generally not very large in the open oceans except at earthquake centres and it could be easily overshadowed by wind-generated ocean surface waves and storm surges. The advance of satellite technique has given us the few rare chances to catch some glimpse of tsunami waves in open oceans. For instance, there were 4 satellites flying over the Indian Ocean during the 26 December 2004 Indian Ocean tsunami period. Smith et al. (2005) extracted the tsunami wave heights from the radar altimeter observations of these satellites by comparing the surface wave observations on that day with previous observations of these satellites 10 to 35 days before the tsunami to remove most of the permanent and slowly varying features of sea level. Although the results are not the “true” tsunami waves due to the difficulties to separate them from other waves and sea level changes, they are the “best” estimations of open-ocean tsunami achievable with the current technology.

In their Fig.1, Smith et al. (2005) show their modelled tsunami waves overlaid with satellite tracks and along track altimeter sea height deviations compared with their modelled tsunami wave heights. Among the 4 satellites, the Envisat satellite observations have the best spatial and temporal coverage of the event. Fig.20 here shows the SMC251020 model simulated tsunami wave field at 3.25 hr after the earthquake and the wave heights along the satellite track, in the same scale as used in the B and F panels of Fig.1 in Smith et al. (2005), which are adapted into the lower two panels in Fig.20 for the convenience of comparison. The B panel of Smith et al. (2005) shows the MOST tsunami model output at 3:15 or 3.25 hr after the 2004 Indian Ocean earthquake. By a visual comparison of the modelled tsunami wave field in the top panel of Fig.20 with the B panel of Smith et al. (2005), it is easy to see that the two simulated tsunami fields share very similar patterns though the present model wave heights are slightly lower than the MOST model output. This is quite encouraging and may be considered one supporting evidence of the present tsunami model. The descending Envisat satellite track spanned over the tsunami wave area in about 10° longitude from 92° to 82° E with a travel time about 2400 s. Assuming the 3.25 hr after the earthquake as the time at the track centre, the start time at the top of track will be 1200 s ahead or 3.05 hr from the earthquake. When the satellite reached the south end of the track it is estimated to be 3.45 hr after the earthquake.

Model wave heights in cells along the Envisat satellite track were interpolated in time with output centred at 3.25 hr or 390 timestep. The cells covered along the Satellite track are marked by the red \* markers in the top panel of Fig.20. Comparing the modelled tsunami waves in the middle panel of Fig.20 with the satellite observations in the F panel of Smith et al. (2005) in the lower panel reveals that this model simulated wave pattern is close to the observed one along the Envisat track though the magnitude is smaller than the observation. The satellite observed maximum wave height along the track is on the order of 0.5 m while the modelled maximum wave height is just about 0.14 m, about 1/3 of the observed one. Note that the satellite observations are 3 hrs after the earthquake and the observations should be treated as far-field observations though the shortest distance from the Satellite track to the epicentre is about 500 km. Also note the present model wave height along the satellite track matches with the satellite peaks and troughs even better than the MOST model output apart from the reduced magnitude. This is probably because the initial earthquake disturbance was not fully known by that time as stated in Smith et al. (2005). The initial condition used in this model simulation is a well-tested one though the initial momentum disturbance is not used.

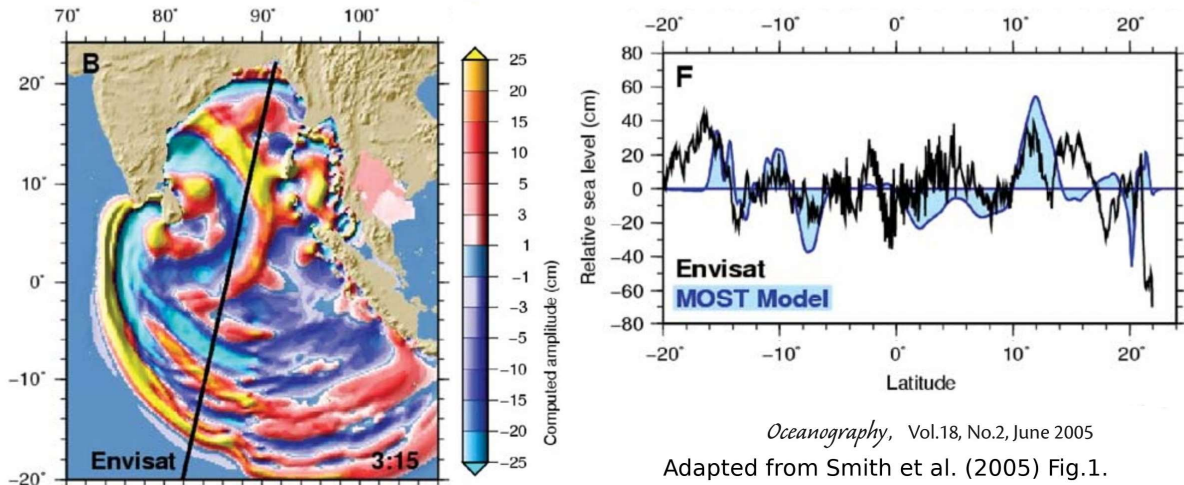
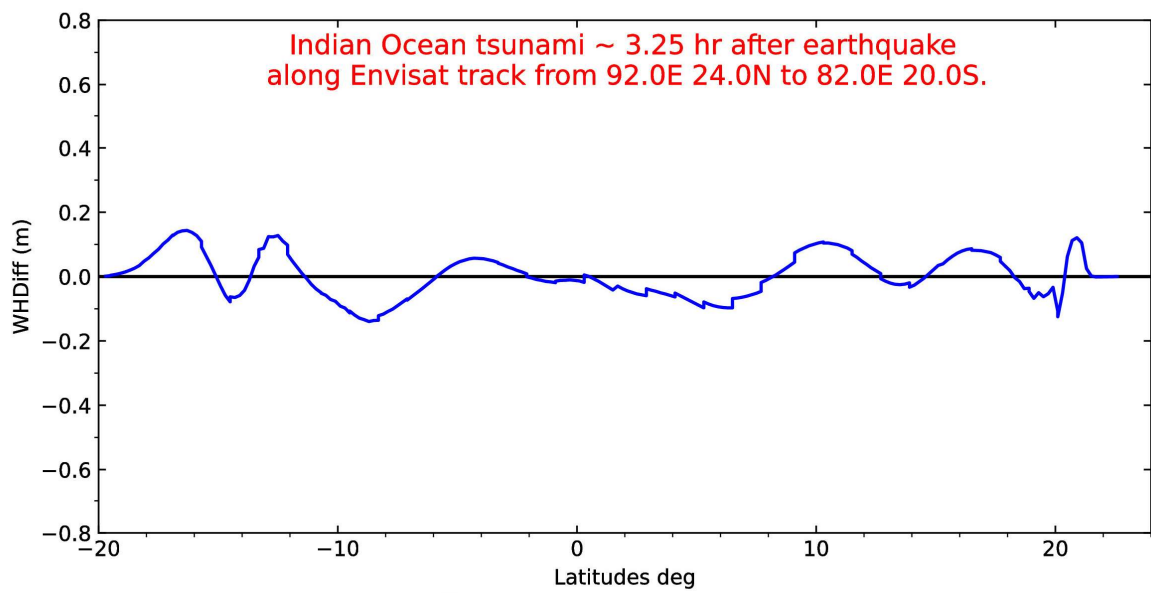
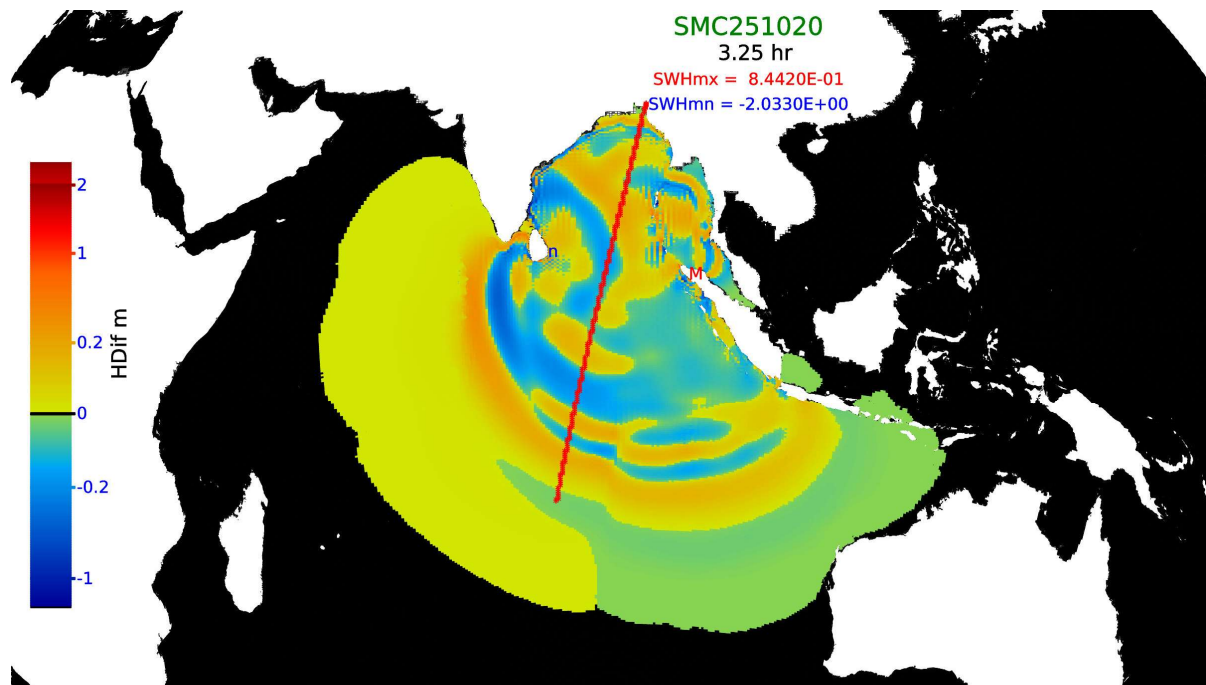


Fig.20 Model simulated tsunami wave height at 3.25 hr after the 2004 Indian Ocean tsunami (top panel) and along the Envisat satellite track (bottom panel), for comparison with the Fig.1 of Smith et al (2005).

Synolakis and Kong (2006) summarised runup measurements about the 2004 Indian Ocean tsunami in other areas, including the worst hit area of Banda Aceh, northeast coast of Sumatra, and other coastal areas of the Indian Ocean. Reported tsunami waves at the Aceh coast were over 9 m high at shore and penetrated inland more than 4 km. An international tsunami survey team (ITST) went to south Sri Lanka in January 2005, two weeks after the tsunami event, and surveyed the coastlines around south Sri Lanka to record the inundation inland distances and flood water levels. The NGDC/WDS has compiled runup records of the 26 December 2004 Indian Ocean tsunami event from all over the world and the data set is available online from its web site:

<https://www.ncei.noaa.gov/products/natural-hazards/tsunamis-earthquakes-volcanoes/tsunamis/recent-significant-events>.

Most of these runup records are for inland sites, particularly at the worst hit area of Aceh, Sumatra, Indonesia. These inland sites are not resolved by the SMC251020 grid due to its coarse resolution of 2.5 km near coastlines. Only 64 records are covered within the SMC251020 grid, and they are used for validation of this model. The numbered marks in Fig.16 indicate the 64 selected sites of runup observations for the 2004 Indian Ocean tsunami. Four extra sites (No. 65-68) are added to show the typical tsunami waves near coastlines though there are no runup records at them, including one near the worst hit Aceh area (No. 66) and one close to Hambantota, the direct hit area of highest casualties in Sri Lanka. The runup records include both maximum wave heights and their arrival times.

Fig.21 shows the time series of simulated tsunami wave heights at 6 selected sites. The Banda, Aceh site (No. 66) is a sea point at 95.1° E, 5.2° N near the coast of Banda. It is within the earthquake-stricken area with an initial water level drop of 1.6 m. The model shows a peak of over 4.2 m high wave arrived at this site in about 30 min after the earthquake. This high wave in the sea could generate higher runup records when it slowed down while travelled further east to the inland Aceh area. The highest recorded runup in the NGDC/WDS observations for the Aceh area is 29 m at 95.235° E 5.495° N. Note the second peak appeared at this site about 2 hours later is about 1.4 m, even higher than all the peak heights shown at other selected sites in this diagram. At the Hambantota site (No. 65) about 81.0° E 6.1° N the model shows two high waves about 1 m high arrived about 2.5 and 3.5 hr after the earthquake and an over 1.5 m drop of water level in-between. The NGDC/WDS records show over 10 m runup at 81.126° E 6.125° N, which is on the coast land in Hambantota, Sri Lanka. The site 30 at Tamil Nadu, India, site 29 near Colombo, Sri Lanka, and site 25 near one of the Maldives islands are all sea points and have runup records for this tsunami event.

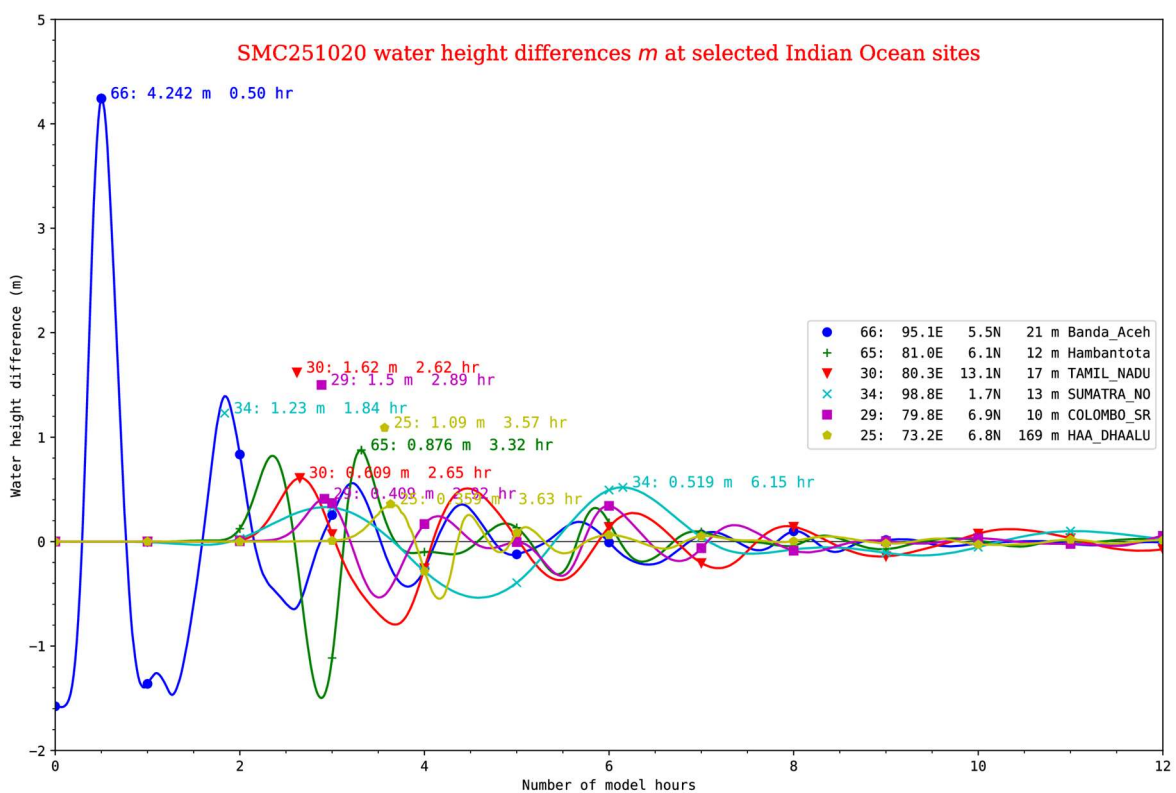


Fig.21 Simulated wave height at 6 selected points for 26 Dec 2004 Indian Ocean tsunami.

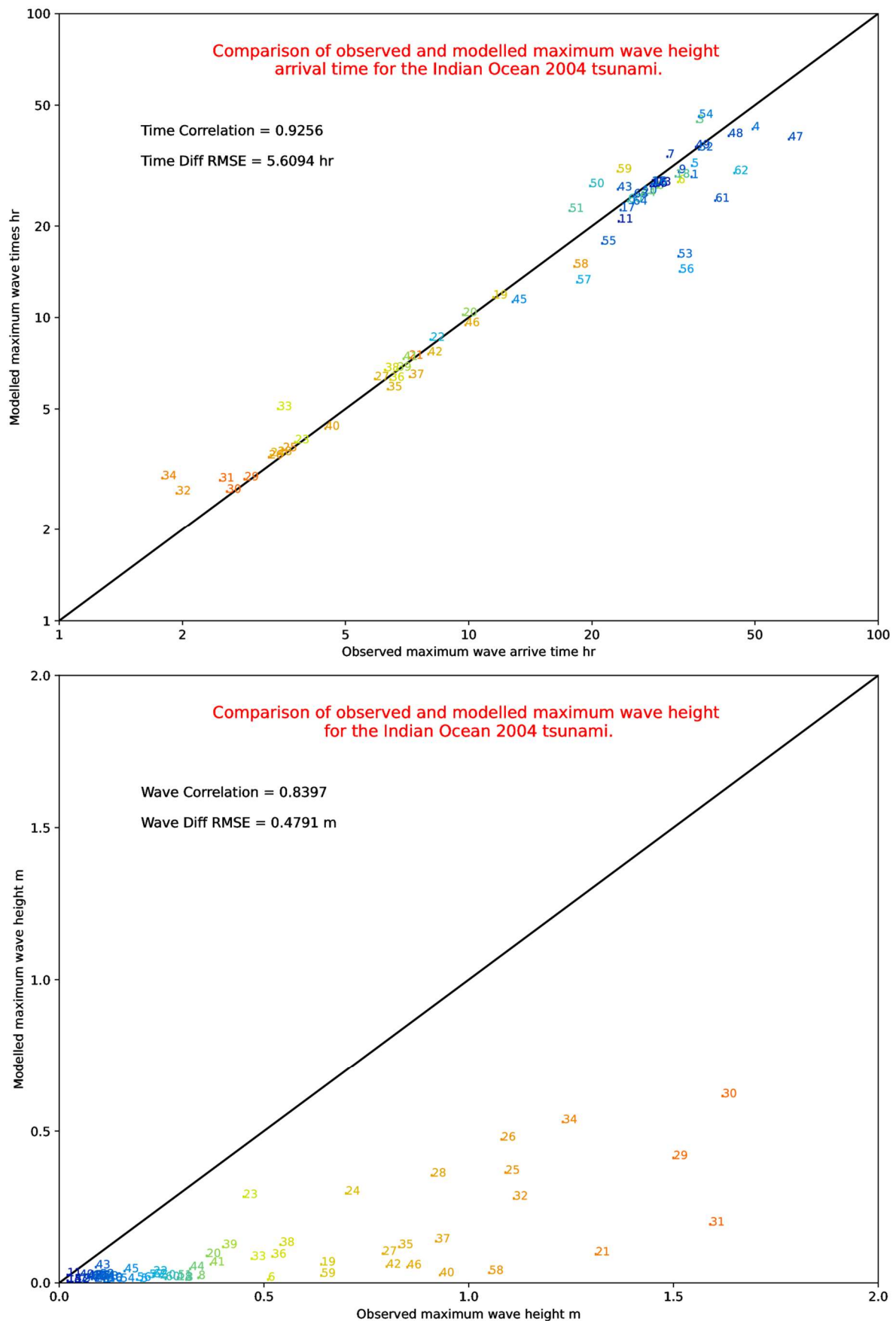


Fig.22 Comparison of modelled tsunami arrival time and maximum wave heights with observations for the 2004 Indian Ocean tsunami.

Their observed wave heights and arrive times are marked with their site number and corresponding line symbols in Fig.21. The modelled time series of wave heights at these sites are shown by the curves with corresponding symbols and their peak values and arrival times are also marked for comparison with the observations. At these 3 sites, the modelled arrival times are quite close to the observed ones (2.62 via 2.65 hr at site 30, 2.89 via 2.92 hr at site 29, and 3.57 via 3.63 hr at site 25), while the wave heights are underestimated by the model, nearly 1/3 of the runup records (1.62 via 0.61 m, 1.5 via 0.41 m, and 1.09 via 0.36 m, respectively). At site 34 North Sumatra, Indonesia, the modelled wave curve has the maximum wave height at the second peak ( $\sim 0.52$  m at 6.15 hr), while the first peak time ( $\sim 3$  hr) is closer to the observed arrival time (1.84 hr) than the maximum wave arrival time. Both modelled peak values (0.33 and 0.52 m) are lower than the recorded runup (1.23 m). This indicates that some observed arrival time may not be the simulated maximum peak time but the first peak time. For this reason, either the modelled first or the maximum peak is selected for comparison with the observed runup wave height and arrival time, whichever is closer to the observed arrival time.

Fig.22 shows the scatter plots of the selected 64 runup observations with modelled peak wave arrival times (top panel) and tsunami wave heights (bottom panel). The modelled tsunami peak arrival times agree well with the observations with a correlation as high as 0.926. The root-mean-square error (RMSE) of 5.61 hr is large, but this value is reasonable considering the long distances of some observations from the epicentre and the possible errors due to local sheltering of the small tsunami waves. At the 64 sites, the modelled tsunami wave heights at the closest grid cells are smaller than the runup observations by a factor of 2 or 3 as shown in the wave height scatter plot (Fig.22 bottom panel). Part of the discrepancy is expected as shoaling of tsunami waves is significant and runup is larger than corresponding open ocean wave height. Nevertheless, model results still show a good correlation with the observations with a coefficient of 0.84. These comparison results confirm that the model is capable of simulating propagations of tsunami waves over the global ocean surfaces despite of underestimation of the wave heights. The modelled peak wave arrival times are close to observations and could be used for development of tsunami warning systems. Possible reasons for the underestimation of tsunami wave heights may be due to the additional diffusion term and the second order advection scheme used in the water height equation.

Popinet (2011) showed that the ‘minmod’ scheme tends to be too dissipative for realistic tsunami modelling though it is very stable and gives reasonable results for dissipative systems. The UNO2 scheme (Li 2008) used in this model is a modification of the ‘minmod’ scheme. Heinrich et al. (2001) simulated the 1998 Papua New Guinea tsunami with a SWEs model, including a bottom friction term as a viscous flow. They stated that high resolution bathymetry up to 5 m accuracy and horizontal mesh close to 100 m resolution in the coastal area may be necessary to simulate the tsunami inundation. The 2.5-km horizontal resolution of the SMC251020 grid is too coarse for this purpose. Behrens and Dias (2015) reviewed numerical simulation of tsunami waves and pointed out that accurate simulation of tsunami wave is quite demanding due to its large span of spatial and temporal scales. In deep ocean, tsunami wave propagation may be approximated by shallow water equations but its transition to a bore or solitary wave train in shelf areas and then into breaking wave in coastal regions demands other mathematical and numerical treatments. The COMCOT model (Wang and Power, 2011) adopted this separate treatment idea for deep and shallow waters and is a good example to follow for improvement of the present SMC grid tsunami model. As the unstructured SMC grid uses nested loops for different sized cells, it would be convenient to apply the coastal scheme to refined cells which are near coastlines; while the linear SWE scheme is kept for the base resolution cells which are in open ocean area and usually in deep waters. Thus, it may form a single model with mixed deep and shallow water schemes and multiple resolutions. This further development is, however, left for interested readers.

## 8. Summary and conclusions

The shallow water equations (SWEs) are discretized on a spherical multiple-cell (SMC) grid and validated with classical tests. The SMC grid is an unstructured latitude-longitude grid and retains finite different schemes on conventional latitude-longitude grid. It uses merged cells at high latitudes to relax the CFL restriction on Eulerian transport schemes and redefines vector components by a fixed reference direction near the poles to avoid the vector polar problem associated with the increased curvature and large mesh stride near the poles. Polar cells centred at the poles are introduced to remove the polar singularity and the polar regions (where the fixed reference direction is used) are separated from the low latitude region (where the local east reference direction is used) by two-way boundary conditions on overlapped rows. The A-grid discretization is applied on prognostic variables of the SWEs, and cell centre velocity is interpolated onto cell faces using a weighted interpolation. The momentum equations are estimated with semi-implicit schemes and an 1-2-1 weighted average is applied on each dimension at an optimized interval so that small scale numerical noises are suppressed just enough to keep the model stable. Mass conservation equation is solved with a non-oscillatory advection scheme with interpolated C-grid velocities and a polar biased diffusion term is added for smoothing. Semi-implicit schemes are used for both the Coriolis

terms and the potential energy gradients. Flux form finite-volume formulations are included for multi-resolution interfaces and applications of different boundary conditions on the SMC grid are explained. For this SWEs model, vertical wall boundary conditions are applied on all boundary faces and any wet cell face bounded by a dry cell whose floor is higher than the water surface of the wet cell. This extended boundary condition allows any cell on this SMC grid to flip between wet and dry states if required. Momentum calculations over dry cells are simply skipped and smoothing is restricted among wet cells for conservation purposes.

The SWEs model is validated with five classic tests on full global grids, including steady zonal flows over flat or hill floor, Rossby-Haurwitz wave and unstable zonal jet. The results demonstrate that the two reference directions work fine on the SMC grid to suppress numerical errors associated with the vector polar problem and the SWEs model is stable if numerical noises are suppressed with enough smoothing. This implies that reduced grids could be reclaimed for dynamical models if the vector polar problem is properly tackled. The unstructured SMC grid also supports multi-resolutions in the mesh refinement style and a refined area is included to show grid refinement effects. For steady smooth flows, the refinement is almost unnoticeable while in unstable jet case, it may stir up instability ripples in the jet flow. This is confirmed by the same test on a single-resolution SMC grid where the zonal jet may be kept stable if the intended initial disturbance is excluded. So, caution should be exercised in multi-resolution grid when strong currents or air jets are involved though the effect needs to be investigated further in details.

The SWEs model is also tested in a 4-level resolution (3-6-12-25 km) regional grid, covering the Mediterranean Sea, and a 4-level (2.5-5-10-20 km) global grid. An experiment of filling the Mediterranean Sea basins is used to test the model boundary conditions and results demonstrate that the filling processes agree well with expectations. The whole Mediterranean Sea is filled up to the sea level in about one month by water from river mouths and strait channels. Total water volume amounts to about 94 m sr, or about 7.5 m deep if the Mediterranean Sea water is evenly spread over the full earth surface. Another experiment is conducted to simulate tsunami waves caused by initial water surface disturbances in the Mediterranean Sea. It was shown that tsunami waves could travel at about 170 m s<sup>-1</sup> and reach Mediterranean coastlines in roughly 4 hr if an earthquake disturbance occurred in the Ionian Sea. The experiment also revealed that orientation of the initial disturbance has profound influence on the subsequent tsunami waves. The coastal surges caused by the initial disturbances are quite small and surge inundations are only revealed by a few coastal cells with floor elevations aligned at the sea level.

The 26 December 2004 Indian Ocean tsunami is simulated with SWEs model on a global 4-level (2.5-5-10-20 km) SMC grid and compared with available observations. The initial seafloor deformation of the earthquake is transformed into an equivalent initial water surface disturbance following a source model, but the momentum of sea water caused by the earthquake is not considered. The modelled tsunami arrival times agree well with observations though tsunami wave heights are underestimated, particularly in the far field. One possible reason for the underestimation is the model smoothing scheme, which consists of an isotropic diffusion term in the mass equation and a weighted average scheme for the momentum equations to suppress numerical short waves. Another reason is the limitation of the linear SWEs to describe coastal bores and breaking waves in shallow waters and on coastal lands. The 2.5 km spatial resolution along coastline is still too coarse for resolving the tsunami runup on coastal lands and the 20 km base resolution in deep oceans could not resolve tsunami of wavelength shorter than about 50 km. Nevertheless, the model shows great potential to simulate tsunami propagation over the whole global ocean surfaces and further increase of spatial resolution may enhance its wave height prediction. If a non-linear scheme could be applied to refined cells, the model may perform better for coastal runup an the present linearized schemes. This is a possible target for future improvement.

## References

- Audusse, E., F. Bouchut, M.O. Bristeau, R. Klein, B. Perthame, 2004. A fast and stable well-balanced scheme with hydrostatic reconstruction for shallow water flows. SIAM J. Sci. Comput. 25, 2050-2065.
- Berger, M.J., D.L. George, R.J. LeVeque, K.T. Mandli, 2011: The GeoClaw software for depth-averaged flows with adaptive refinement. Adv. Water Resources, 34, 1195-1206. doi: 10.1016/j.advwatres.2011.02.016.
- Berger, M., J. Oliger, 1984. Adaptive mesh refinement for hyperbolic partial differential equations. J. Comput. Phys. 53, 484-512.
- Behrens, J., F. Dias, 2015. New computational methods in tsunami science. Philosophical Transactions A, 373, 20140382.
- Courtier, P., M. Naughton 1994: A pole problem in the reduced Gaussian grid. Q.J.R. Meteorol. Soc. 120, 1389-1407.
- Cullen, M.J.P. 1974: Integrations of the primitive equations on a sphere using the finite-element method. Q.J.R. Meteorol. Soc. 100, 555-562.
- Duben, P.D., P. Korn, V. Aizinger 2012: A discontinuous/continuous low order finite element shallow water model on the sphere. J. Comput. Phy. 231, 2396-2413.
- Galewsky, J., R.K. Scott, L.M. Polvani 2004: An initial-value problem for testing numerical models of the global shallow-water equations. Tellus 56A, 429-440.

- Gates, W.L., C.A. Riegel, 1962. A study of numerical errors in the integration of barotropic flow on a spherical grid. *J. Geophys. Res.* 67, 773-784.
- Giraldo, F.X., J.S. Hesthaven, T. Warburton 2002: Nodal high-order discontinuous Galerkin methods for the spherical shallow water equations. *J. Comput. Phys.* 181, 499-525.
- Glahn, B., A. Taylor, N. Kurkowski, W.A. Shaffer, 2009. The Role of the SLOSH Model in National Weather Service Storm Surge Forecasting. *National Weather Digest* 33 (1), 3-14.
- Grilli, S.T., M. Ioualalen, J. Asavanant, F. Shi, J.T. Kirby, P. Watts, 2007: Source Constraints and Model Simulation of the December 26, 2004, Indian Ocean Tsunami. *J. Waterway, Port, Coastal, Ocean Eng.* 133(6), 414-428.
- Heikes, R., D.A. Randall 1995: Numerical integration of the shallow-water equations on a twisted icosahedral grid, Part I. and II. *Mon. Wea. Rev.* 123, 1862-1887.
- Heinrich, Ph., A. Piatanesi, H. Hebert, 2001. Numerical modelling of tsunami generation and propagation from submarine slumps: the 1998 Papua New Guinea event. *Geophys. J. Int.* 145, 97-111.
- Hollingsworth, A., P. Kallberg, V. Renner, D.M. Burridge, 1983. An internal symmetric computational instability. *Q.J.R. Meteorol. Soc.* 109, 417-428.
- Hortal, M., A.J. Simmons 1991: Use of reduced Gaussian grids in spectral models. *Mon. Wea. Rev.* 119, 1057-1074.
- Kageyama, A., T. Sato 2004: The Yin-Yang grid: An overset grid in spherical geometry. *Geochem. Geophys. Geosyst.* 5, Q09005, doi:10.1029/2004GC000734.
- Kent, J., C. Jablonowski, J. Thuburn, N. Wood 2016: An energy-conserving restoration scheme for the shallow-water equations. *Q.J.R. Meteorol. Soc.* 142, 1100-1110.
- Klepitskova, O., J.D. Pietrzak, G.S. Stelling 2009: On the accurate and stable reconstruction of tangential velocities in C-grid ocean models. *Ocean Modelling* 28, 118-126.
- Kurihara, Y. 1965: Numerical integration of the primitive equations on a spherical grid. *Mon. Wea. Rev.* 93, 399-415.
- LeVeque, R.J., D.L. George, M.J. Berger, 2011. Tsunami modelling with adaptively refined finite volume methods. *Acta Numerica* 20, 211-289. DOI:10.1017/S0962492911000043
- Li, J.G. 2003: Multiple-cell flat-level model for atmospheric tracer dispersion over complex terrain. *Boundary-Layer Meteorology*, 107, 289-322. DOI:10.1023/A:1022115808637.
- Li, J.G. 2008: Upstream nonoscillatory advection schemes. *Mon. Wea. Rev.*, 136, 4709-29. DOI: 10.1175/2008MWR2451.1
- Li, J.G. 2011: Global transport on a spherical multiple-cell grid. *Mon. Wea. Rev.*, 139, No.5, 1536-1555. DOI: 10.1175/2010MWR3196.1.
- Li, J.G. 2012: Propagation of Ocean Surface Waves on a Spherical Multiple-Cell Grid. *J. Comput. Phys.*, 231, 8262-8277. DOI: 10.1016/j.jcp.2012.08.007.
- Li, J.G. 2016: Ocean surface waves in an ice-free Arctic Ocean. *Ocean Dynamics*, 66, 989-1004. DOI:10.1007/s10236-016-0964-9.
- Li, J.G. 2018: Shallow-water equations on a spherical multiple-cell grid. *Q.J. Royal Meteorol. Soc.*, 144, 1-12. DOI: 10.1002/qj.3139.
- Li, J.G. 2021: Filling oceans on a spherical multiple-cell grid. *Ocean Modelling*, 157, 101729. DOI: 10.1016/j.ocemod.2020.101729.
- Li, J.G. 2022: Hybrid multi-grid parallelisation of WAVEWATCH III model on spherical multiple-cell grids. *J. Parallel Distrib. Comput.*, 167C, 187-198. DOI: 10.1016/j.jpdc.2022.05.002
- Li, J.G., A. Saulter 2014: Unified global and regional wave model on a multi-resolution grid. *Ocean Dynamics*, 64, 1657-1670. DOI: 10.1007/s10236-014-0774-x.
- Li, J.G., P. Wang 2024: Global tsunami modelling on a spherical multiple-cell grid. *Ocean Modelling*, 192, 102461. doi: 10.1016/j.ocemod.2024.102461.
- Lin, S.-J., R. B. Rood 1997: An explicit flux-form semi-Lagrangian shallow-water model on the sphere. *Q.J.R. Meteorol. Soc.* 123, 2477-2498.
- McDonald, A., J.R. Bates 1989: Semi-Lagrangian integration of a grid point shallow water model on the sphere. *Mon. Wea. Rev.* 117, 130-137.
- Mohebalhojeh, A.R., D.G. Dritschel 2000: On the representation of gravity waves in numerical models of the shallow-water equations. *Q.J.R. Meteorol. Soc.* 126, 669-688.
- Musinguzi, A., M.K. Akbar, J.G. Fleming, S.K. Hargrove, 2019. Understanding hurricane storm surge generation and propagation using a forecasting model, forecast advisories and best track in a wind model, and observed data - case study Hurricane Rita. *J. Marine Sci. Eng.* 7, 77. 30pp.
- Nair, R.D., S.J. Thomas, R.D. Loft 2005: A discontinuous Galerkin global shallow water model. *Mon. Wea. Rev.* 133, 876-888.
- National Geophysical Data Center / World Data Service: NCEI/WDS Global Historical Tsunami Database. NOAA National Centers for Environmental Information. doi:10.7289/V5PN93H7.
- Okada, Y., 1985: Surface deformation due to shear and tensile faults in a half-space. *Bull. Seism. Soc. Am.*, 75(4): 1135–1154. doi: 10.1785/BSSA0750041135.
- Okada, Y., 1992: Internal deformation due to shear and tensile faults in a half-space, *Bull. Seism. Soc. Am.*, 82(2), 1018-1040. doi: 10.1785/BSSA0820021018.
- Peixoto, P.S., S.R.M. Barros 2013: Analysis of grid imprinting on geodesic spherical icosahedral grids. *J. Comput. Phys.* 237, 61-78.
- Pietrzak J., A. Socquet, D. Ham, W. Simons, C. Vigny, R.J. Labeur, E. Schrama, G. Stelling, D. Vatvani, 2007: Defining the source region of the Indian Ocean Tsunami from GPS, altimeters, tide gauges and tsunami models. *Earth & Planetary Science Letters* 261, 49-64.
- Popinet, S., 2011: Quadtree-adaptive tsunami modelling. *Ocean Dynamics* 61, 1261-1285.
- Popinet, S., R.M. Gorman, G.J. Rickard, H.L. Tolman, 2010: A quadtree-adaptive spectral wave model, *Ocean Model.* 34, 36-49.

- Popinet, S., Rickard, G., 2007. A tree-based solver for adaptive ocean modelling. *Ocean Model.* 16, 224-249.
- Purser, R.J., M. Rancic 1997: Conformal octagon: an attractive framework for global models offering quasi-uniform regional enhancement of resolution. *Meteorol. Atmos. Phys.* 62, 33-48.
- Qaddouri, A., J. Pudykiewicz, M. Tanguay, C. Girald, J. Cote 2012: Experiments with different discretizations for the shallow-water equations on a sphere. *Q.J.R. Meteorol. Soc.* 138, 989-1003.
- Rancic, M., R.J. Purser, F. Mesinger 1996: A global shallow-water model using an expanded spherical cube: Gnomonic versus conformal coordinates. *Q.J.R. Meteorol. Soc.* 122, 959-982.
- Rancic, M., H. Zhang, V. Savic-Jovicic 2008: Nonlinear advection schemes on the octagonal grid. *Mon. Wea. Rev.* 136, 4668-4686.
- Ringler, T.D., D. Jacobsen, M. Gunzburger, L. Ju, M. Duda, W. Skamarock 2011: Exploring a multiresolution modeling approach within the shallow-water equations. *Mon. Wea. Rev.* 139, 3348-3368.
- Ringler, T.D., J. Thuburn, J.B. Klemp, W.C. Skamarock 2010. A unified approach to energy conservation and potential vorticity dynamics for arbitrarily-structured C-grids. *J. Comput. Phys.* 229, 3065-3090.
- Sadourny, R. 1972: Conservative finite-difference approximations of the primitive equations on quasi-uniform spherical grids. *Mon. Wea. Rev.* 100, 136-144.
- Sadourny, R., A. Arakawa, Y. Mintz 1968: Integration of the nondivergent barotropic vorticity equation with an icosahedral-hexagonal grid for the sphere. *Mon. Wea. Rev.* 96, 351-356.
- Shuman, F.G. 1970: On certain truncation errors associated with spherical coordinates. *J. Appl. Meteorol.* 9, 564-570.
- Smith, W.H.F., R. Scharroo, V.V. Titov, D. Arcas, B.K. Arbic, 2005: Ocean news: Satellite altimeters measure tsunami - Early model estimates confirmed. *Oceanography* 18(2), 11-13, doi: 10.5670/oceanog.2005.62.
- Staniforth, A., J. Thuburn 2012: Horizontal grids for global weather and climate prediction models: a review. *Q.J.R. Meteorol. Soc.* 138, 1-26.
- St-Cyr, A., C. Jablonowski, J.M. Dennis, H.M. Tufo, S.J. Thomas 2008: A comparison of two shallow-water models with nonconforming adaptive grids. *Mon. Wea. Rev.* 136, 1898-1922.
- Swinbank, R., R.J. Purser 2006: Fibonacci grids: a novel approach to global modelling. *Q.J.R. Meteorol. Soc.* 132, 1769-1793
- Synolakis, C.E., E.N. Bernard, 2006: Tsunami science before and beyond Boxing Day 2004. *Phil. Trans. R. Soc. A*, 364, 2231-2265. DOI:10.1098/rsta.2006.1824
- Synolakis, C.E., and L. Kong, 2006: Runup Measurements of the December2004 Indian Ocean Tsunami. *Earthquake Spectra*, 22 (Suppl. 3), S67-S91.
- Thuburn, J., Y. Li 2000: Numerical simulations of Rossby-Haurwitz waves. *Tellus* 52A, 181-189.
- Walters, R.A., E. Hanert, J. Pietrzak, D.Y. Le Roux 2009: Comparison of unstructured, staggered grid methods for the shallow water equations. *Ocean Modelling* 28, 106-117.
- Wang, X., W. Power, 2011: COMCOT: a Tsunami Generation Propagation and Run-up Model. *GNS Sci. Report* 2011/43, 129pp.
- WAVEWATCH III Development Group (WW3DG), 2019: User manual and system documentation of WAVEWATCH III version 6.07. Tech. Note 333, NOAA/NWS/NCEP/MMAB, College Park, MD, USA, 465 pp. + Appendices. <https://github.com/NOAA-EMC/WW3/releases/tag/6.07>
- Weller, H., J. Thuburn, C.J. Cotter 2012: Computational modes and grid imprinting on five quasi-uniform spherical C grids. *Mon. Wea. Rev.* 140, 2734-2755.
- Weller, H., H.G. Weller, A. Fournier 2009: Voronoi, Delaunay, and block-structured mesh refinement of solution of the shallow-water equations on the sphere. *Mon. Wea. Rev.* 137, 4208-4224.
- Williamson, D.L. 1968: Integration of the barotropic vorticity equation on a spherical geodesic grid. *Tellus* 20, 642-653.
- Williamson, D.L., G.L. Browning 1973: Comparison of grids and difference approximations for numerical weather prediction over a sphere. *J. Appl. Meteorol.* 12, 264-274.
- Williamson, D.L., J.B. Drake, J.J. Hack, R. Jakob and P.N. Swarztrauber 1992: A standard test set for numerical approximations to the shallow-water equations in spherical geometry. *J. Comput. Phys.* 102, 221-224.
- Williamson, D.L., J.M. Rosinski 2000: Accuracy of reduced-grid calculations. *Q.J.R. Meteorol. Soc.* 126, 1619-1640.
- Zhang, Y.J., G. Priest, J. Allan, L. Stimely, 2016: Benchmarking an Unstructured-Grid Model for Tsunami Current Modeling. *Pure Appl. Geophys.*, 173, 4075-4087. doi: 10.1007/s00024-016-1328-6.